



A reduced 3D-0D fluid–structure interaction model of the aortic valve that includes leaflet curvature

Ivan Fumagalli¹ · Luca Dede¹ · Alfio Quarteroni^{1,2}

Received: 18 November 2024 / Accepted: 5 April 2025
© The Author(s) 2025

Abstract

We introduce an innovative lumped-parameter model of the aortic valve, designed to efficiently simulate the impact of valve dynamics on blood flow. Our reduced model includes the elastic effects associated with the leaflets' curvature and the stress exchanged with the blood flow. The introduction of a lumped-parameter model based on momentum balance entails an easier calibration of the model parameters: Phenomenological-based models, on the other hand, typically have numerous parameters. This model is coupled to 3D Navier–Stokes equations describing the blood flow, where the moving valve leaflets are immersed in the fluid domain by a resistive method. A stabilized finite element method with a BDF time scheme is adopted for the discretization of the coupled problem, and the computational results show the suitability of the system in representing the leaflet motion, the blood flow in the ascending aorta, and the pressure jump across the leaflets. Both physiological and stenotic configurations are investigated, and we analyze the effects of different treatments for the leaflet velocity on the blood flow.

Keywords Cardiac valve dynamics · Computational fluid dynamics · Reduced fluid–structure interaction · Lumped-parameter model · Resistive immersed implicit surface · Aortic valve stenosis

1 Introduction

Cardiac valves allow maintaining unidirectional blood flow in the heart and circulatory system. Their function helps in reducing blood stagnation by improving the chamber wash-out and in directing the ejection jets and the coherent vortex structures of the flow. Because of the relevance of such components, several cardiac pathologies are directly related (or at least entail) valvular abnormal conditions, such as calcification, stenosis, regurgitation, and anatomical defects of the leaflets or the subvalvular apparatus: see, e.g., (Schoen 2005; Otto 2008; Xanthos et al. 2011; El Sabbagh et al. 2018).

Due to the complexity of cardiac valve structure and their strong interplay with blood flow, valve modeling in computational hemodynamics has been developed with different levels of detail. Several works consider a prescribed kinematics of the valves, introducing interface conditions that are expressed by analytical laws, as in Mihalef et al. (2011), Seo et al. (2014), Tagliabue et al. (2017a), Tagliabue et al. (2017b), Zingaro et al. (2021), Zingaro et al. (2022), or derived from clinical measurements, as in Viscardi et al. (2010), Chnafa et al. (2014), Bonomi et al. (2015), Chnafa et al. (2016), This et al. (2020). On the other hand, detailed mechanical models for the leaflets have also been proposed in the literature, possibly including the inhomogeneities and the fibers in the leaflets (see, e.g., (Marom et al. 2013; Marom 2015; Kaiser et al. 2021)) or a mechanical coupling with the subvalvular apparatus and the proximal vessels, such as in Kunzelman and Cochran (1990), Rim et al. (2014), Schievano et al. (2007), Bellhouse (1969), Moore et al. (2013). In order to couple such complex models with hemodynamics, the solution of a three-dimensional fluid–structure interaction (FSI) problem is required. A wide range of numerical methods have been employed to this aim (Quarteroni et al. 2019; Fumagalli and Vergara 2024), either

✉ Ivan Fumagalli
ivan.fumagalli@polimi.it

Luca Dede¹
luca.dede@polimi.it

Alfio Quarteroni
alfio.quarteroni@polimi.it

¹ MOX, Dipartimento di Matematica, Politecnico di Milano, piazza Leonardo da Vinci 32, 20133 Milan, Italy

² Institute of Mathematics, École Polytechnique Fédérale de Lausanne, Route Cantonale, 1015 Lausanne, Switzerland

in a boundary-fitting setting or from a Eulerian standpoint: the Arbitrary Lagrangian–Eulerian scheme (Cheng et al. 2004; Jianhai et al. 1996; Espino et al. 2014; Basting et al. 2017; Nestola et al. 2017), the CUTFEM and XFEM methods (Alauzet et al. 2016; Hansbo et al. 2015; Burman and Fernández 2014; Gerstenberger and Wall 2010; Mayer et al. 2010; Massing et al. 2015; Gerstenberger and Wall 2008; Formaggia et al. 2018; Zonca et al. 2018), the immersed boundary (Peskin 1972; Liu et al. 2006; Borazjani et al. 2008, 2010; Ge and Sotiropoulos 2010; Griffith et al. 2009; Griffith 2012; Votta et al. 2013; Hsu et al. 2014; Wu et al. 2018; Yang et al. 2018; Nestola et al. 2019) and the fictitious domain approach (Glowinski et al. 1997; van Loon et al. 2006; Dos Santos et al. 2008; Astorino et al. 2009; Bazilevs et al. 2011; Kamensky et al. 2015; De Hart et al. 2003; Stijnen et al. 2004; Morsi et al. 2007), the chimera method (Ge et al. 2005; Zahle et al. 2009; Le and Sotiropoulos 2013), and space-time finite elements (Hughes and Hulbert 1988; Tezduyar and Sathe 2007; Takizawa et al. 2018), to mention a few. The common ground of all these methods is that they require a full 3D (or at least 2D) representation of the valve geometry and of its mechanics solver, thus entailing a significantly increased computational cost with respect to imposed-displacement hemodynamics.

Conversely, in many clinical applications, the primary focus is on blood flow dynamics rather than the stresses and mechanical response of the valves themselves. In this regard, aiming at modeling the valve dynamics with little computational burden, while retaining its interaction with the blood flow, lumped-parameter models have been introduced. Most of such models, e.g., those proposed in Korakianitis and Shi (2006), Blanco et al. (2010), Regazzoni et al. (2022), typically account for the valve hemodynamics effects by means of a phenomenological relationship between the pressure jump across the leaflets and the flowrate passing through them. However, since the parameters appearing in the equations seldom have a precisely quantifiable physical meaning, the calibration of the model may be quite cumbersome and highly dependent on the specific application of interest. Other works derive their reduced model from a momentum balance at the leaflets: Up to the authors' knowledge, this approach has been first adopted by Domenichini and Pedrizetti (2015), where the inertia and stiffness of the leaflets are neglected, while in the more recent work by Seo et al. (2020) a linear ordinary differential equation is introduced for the valve opening coefficient. However, the geometry of the leaflets plays a marginal role in the model, affecting only the valve's inertia.

In this paper, we introduce a novel lumped-parameter structure model for the aortic valve, with the aim of enriching the description of the valve dynamics with respect to other OD models in the literature while preserving a low computational effort compared to fully 3D FSI systems. We

derive our simplified model from the balance of forces at the leaflet, relating the elasticity of the leaflets to their curvature. Although not entailing a locally accurate description of the leaflet mechanics, this approach allows to synthetically account for the specific valve geometry and to relate it directly with the total force exerted by the flow on the leaflets.

Based on this mechanical model, we set up a 3D-0D fluid–structure interaction (FSI) system modeling the interplay between the three-dimensional blood flow in the ascending aorta and the aortic valve dynamics. Blood dynamics is described by incompressible Navier-Stokes equations, and the hemodynamics effect of the valve's kinematics is accounted for by the resistive immersed implicit surface method (RIIS) introduced by Fedele et al. (2017). This method is inspired by the resistive immersed surface (RIS) method by Fernández et al. (2008) and Astorino et al. (2012), it is characterized by a negligible computational overhead cost in CFD simulations, and its suitability for the description of hemodynamics effects of cardiac valves has been shown both in physiological and pathological conditions: see Dedè et al. (2019), Zingaro et al. (2022) and Fumagalli et al. (2020), Fumagalli et al. (2022), respectively. Moreover, the proposed reduced model has also been applied to assess the effects of pulmonary valve replacement on the hemodynamics of the proximal pulmonary arteries (Criseo et al. 2024).

This paper is organized as follows. In Sect. 2, we introduce the FSI mathematical model, made of the novel lumped-parameter structural model of the aortic valve, the blood flow equations including the RIIS representation of the leaflets, and the coupling between the two systems. The numerical approximation of the reduced FSI problem and the scheme for its solution are described in Sect. 2.4. Then, computational results are presented in Sect. 3, including an analysis of the reconstruction of leaflet velocity, the investigation of physiological and pathological conditions, and the comparison with a well-known model available in the literature. These results demonstrate that the proposed model serves as a computationally efficient tool for capturing the effects of valve dynamics on blood flow dynamics and patterns, as well as hemodynamics indicators that are meaningful to address clinical questions.

2 Models and methods

We present a reduced model for the fluid–structure interaction between the blood flow in the aorta and the aortic valve leaflets. In Sect. 2.1, we introduce the fluid dynamics system, with the valve effects modeled by the resistive method of Fedele et al. (2017); Fumagalli et al. (2020). Then, a reduced structure model for valve dynamics is derived in Sect. 2.2,

considering the external forces induced on the leaflets by the surrounding blood, and the FSI coupling is presented in Sect. 2.3.

2.1 Fluid model and RIIS method

We model blood as incompressible and Newtonian, with uniform density ρ and viscosity μ , and the domain Ω of interest is represented in Fig. 1. The effects of the valve on the fluid dynamics are accounted for by the resistive immersed implicit surface (RIIS) method, introduced by Fedele et al. (2017) and employed by Fumagalli et al. (2020), (2022) in a clinical context. This method, based on the resistive immersed surface (RIS) approach proposed by Fernández et al. (2008), Astorino et al. (2009), Astorino et al. (2012), consists in the introduction of an additional penalty term in the fluid momentum equation, thus weakly imposing the kinematic condition at the surface representing the valve.

According to the RIIS method, the geometry of the moving valve Γ_t is represented as a surface immersed in the fluid domain Ω , implicitly described at each time t by a level-set function $\varphi_t : \Omega \rightarrow \mathbb{R}$, as

$$\Gamma_t = \{ \mathbf{x} \in \Omega : \varphi_t(\mathbf{x}) = 0 \}. \tag{1}$$

The function φ_t is assumed to be a signed distance function, namely to fulfill $|\nabla\varphi_t| = 1$, for any t . A smeared Dirac delta function $\delta_{t,\epsilon} : \Omega \rightarrow [0, +\infty)$ is then introduced, to approximate the Dirac distribution—rigorously, the codimension-1 Hausdorff measure—with support on the surface Γ_t , as follows:

$$\delta_{t,\epsilon}(\mathbf{x}) = \begin{cases} \frac{1+\cos(\pi\varphi_t(\mathbf{x})/\epsilon)}{2\epsilon} & \text{if } |\varphi_t(\mathbf{x})| \leq \epsilon, \\ 0 & \text{if } |\varphi_t(\mathbf{x})| > \epsilon, \end{cases} \tag{2}$$

where the half-amplitude ϵ is the smoothing parameter.

In these settings, the velocity \mathbf{u} and pressure p of the blood satisfy the following formulation of the Navier–Stokes equations:

$$\begin{cases} \partial_t \mathbf{u} + \rho \mathbf{u} \cdot \nabla \mathbf{u} - \nabla \cdot \boldsymbol{\sigma} + \frac{R}{\epsilon} (\mathbf{u} - \mathbf{u}_\Gamma) \delta_{t,\epsilon} = \mathbf{0} & \text{in } \Omega, t \in (0, T], \\ \nabla \cdot \mathbf{u} = 0 & \text{in } \Omega, t \in (0, T], \\ \mathbf{u} = \mathbf{0} & \text{on } \Sigma_w, t \in (0, T], \\ \boldsymbol{\sigma} \mathbf{n} = p_{\text{in}} \mathbf{n}, & \text{on } \Sigma_{\text{in}}, t \in (0, T], \\ \boldsymbol{\sigma} \mathbf{n} = p_{\text{out}} \mathbf{n}, & \text{on } \Sigma_{\text{out}}, t \in (0, T], \\ \mathbf{u} = \mathbf{0} & \text{in } \Omega, t = 0, \end{cases} \tag{3}$$

where $\boldsymbol{\sigma} = 2\mu D(\mathbf{u}) - pI = \mu(\nabla\mathbf{u} + \nabla\mathbf{u}^T) - pI$ is the fluid stress tensor, R is the resistance of the RIIS term—acting as a penalty parameter—and \mathbf{u}_Γ is the velocity of the valve, which constitutes a data for the fluid problem and will be discussed in the following sections. Regarding boundary conditions, $p_{\text{in}}, p_{\text{out}}$ are the pressure values imposed at the inflow and outflow boundaries $\Sigma_{\text{in}}, \Sigma_{\text{out}}$, respectively, while the boundary Σ_w represents the aortic wall.

2.2 Lumped-parameters mechanical model

In order to provide the configuration and the velocity of the valve, represented by φ_t and \mathbf{u}_Γ in the fluid problem (3), a structural model would be required for the deformation of the surface Γ_t . This section is devoted to the derivation of a reduced, lumped-parameters model realistically describing the main features of cardiac valve dynamics. The approach

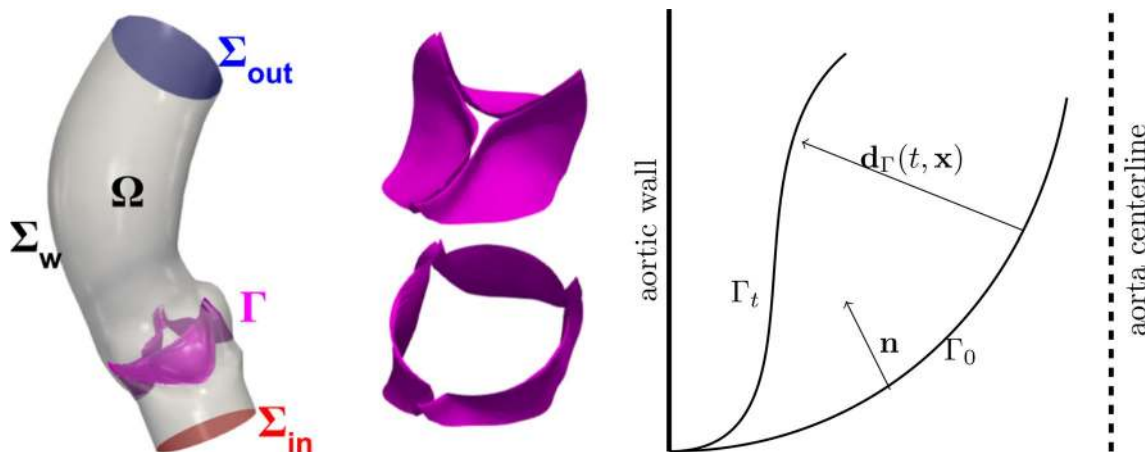


Fig. 1 Computational domain and valve description. Left: the domain Ω with its boundaries and the immersed valve Γ in purple; center: closed (above) and open (below) configuration of the aortic valve; right: schematic representation of a leaflet section and motion

differs from the one proposed by Seo et al. (2020) in that the elastic terms are related to the curvature of the leaflet, thus including additional geometrical information in the model.

Let $\mathbf{d}_\Gamma : [0, T] \times \hat{\Gamma} \rightarrow \mathbb{R}^3$ denote the displacement of the leaflet with respect to its reference configuration $\Gamma_0 = \hat{\Gamma}$, namely we can represent the current configuration Γ_t as

$$\Gamma_t = \{\mathbf{x} \in \mathbb{R}^3 : \mathbf{x} = \mathbf{T}_t(\hat{\mathbf{x}}) = \hat{\mathbf{x}} + \mathbf{d}_\Gamma(t, \hat{\mathbf{x}}) \text{ for some } \hat{\mathbf{x}} \in \hat{\Gamma}\}, \tag{4}$$

as schematically displayed in Fig. 1.

We assume that at each time t , every point $\mathbf{x} \in \Gamma_t$ of the leaflet is subject to an external force $\mathbf{f}(t, \mathbf{x})$ due to the surrounding fluid and to an elastic force related to the leaflet curvature $H(\mathbf{x})$ —both depending on the current configuration of Γ_t , described by $\mathbf{d}_\Gamma(\mathbf{x})$ —and that the valve motion can be affected by some damping effect. Regarding the curvature-induced elastic force, we assume that it acts only normally to the surface, similarly to what happens in free-surface tension (see, e.g., Buscaglia and Ausas 2011; Fumagalli et al. 2018). Moreover, since it is generally observed that the resting state of the aortic valve is its closed configuration; we impose this elastic force to vanish on $\hat{\Gamma}$.

According to these assumptions, a local force balance can be formulated as follows:

$$\rho_\Gamma \ddot{\mathbf{x}} + \beta \rho_\Gamma \dot{\mathbf{x}} = \mathbf{f}(t, \mathbf{x}) - \gamma \left(H(\mathbf{x}) - \hat{H}(\hat{\mathbf{x}}) \right) \mathbf{n}_\Gamma(\mathbf{x}), \tag{5}$$

where ρ_Γ is a parameter accounting for the inertia of the valve leaflets, β is a damping coefficient, γ is an elasticity coefficient, and \mathbf{n}_Γ is the normal to the surface Γ_t . The function $\hat{H}(\hat{\mathbf{x}})$ denotes the total curvature of the surface $\hat{\Gamma}$ in the position $\hat{\mathbf{x}} = \mathbf{T}_t^{-1}(\mathbf{x})$ corresponding to \mathbf{x} , that is the curvature of the resting configuration. The parameter ρ_Γ can be considered an *effective surface density* of the valve, since it accounts for the mass m_Γ of the leaflets through the relation

$$m_\Gamma = \int_\Omega \rho_\Gamma \delta_{t,\varepsilon} d\Omega = \rho_\Gamma |\Gamma_t|.$$

Since we also know that $m_\Gamma = \rho_{\text{valve}} \ell |\Gamma_t|$, where ρ_{valve} is the actual density of the leaflets and ℓ their average thickness, we have $\rho_\Gamma = \rho_{\text{valve}} \ell$. In the following, we consider the common assumption that $\rho_{\text{valve}} = \rho$ and adopt $\ell = 0.25\text{mm}$ as the leaflet thickness (Morganti et al. 2015; Thubrikar 2018). It is worth to point out that the parameter ρ_Γ could also be tuned to different values—without loss of generality—in order to account for the inertia of the leaflets, which may be unknown in patient-specific settings or possibly be affected by added-mass effects (cf., e.g., (Causin et al. 2005)).

Aiming at reducing Eq. (5) to a 0D model, we assume that \mathbf{d}_Γ can be decomposed as

$$\mathbf{d}_\Gamma(t, \hat{\mathbf{x}}) = c(t) \mathbf{g}(\hat{\mathbf{x}}), \tag{6}$$

where the spatial dependence of the displacement, represented by the function $\mathbf{g} : \hat{\Gamma} \rightarrow \mathbb{R}^3$, is known, while the opening coefficient $c : [0, T] \rightarrow \mathbb{R}$ has to be modeled. In these settings, the local balance (5) can be re-written as

$$\begin{aligned} & (\ddot{c}(t) + \beta \dot{c}(t)) \rho_\Gamma \mathbf{g}(\mathbf{T}_t^{-1}(\mathbf{x})) \\ & = \mathbf{f}(t, \mathbf{x}) - \gamma \left(H(\mathbf{x}) - \hat{H}(\mathbf{T}_t^{-1}(\mathbf{x})) \right) \mathbf{n}_\Gamma(\mathbf{x}). \end{aligned} \tag{7}$$

Taking the component along $\mathbf{n}_\Gamma(\mathbf{x})$ and integrating over Γ_t , we obtain the following ordinary differential equation for c :

$$\begin{aligned} & \ddot{c} + \beta \dot{c} + \eta(c, \mathbf{f}) = 0, \quad \text{where} \\ & \eta(c(t), \mathbf{f}(t)) \\ & = \frac{\gamma \int_{\Gamma_t} \left(H(\mathbf{x}) - \hat{H}(\mathbf{T}_t^{-1}(\mathbf{x})) \right) \cdot \mathbf{n}_\Gamma(\mathbf{x}) d\mathbf{x}}{\int_{\Gamma_t} \rho_\Gamma \mathbf{g}(\mathbf{T}_t^{-1}(\mathbf{x})) \cdot \mathbf{n}_\Gamma(\mathbf{x})}, \end{aligned} \tag{8}$$

where the dependence of η on c is implicit in its dependence from the curvature H : indeed, $H = -\text{div}_\Gamma \mathbf{n}_\Gamma$ and the normal vector \mathbf{n}_Γ can be computed in terms of the derivatives of the function $\mathbf{T}_t(\hat{\mathbf{x}}) = \hat{\mathbf{x}} + c(t) \mathbf{g}(\hat{\mathbf{x}})$; a more precise definition of \mathbf{n}_Γ and H will be introduced in Sect. 2.3. Equation (8) can be completed by proper initial conditions on c and \dot{c} , depending on the application of interest.

2.3 Coupling of the fluid and structure models

We couple the 3D fluid model described in Sect. 2.1 and the 0D valve model introduced in Sect. 2.2 to obtain a reduced FSI model: The fluid-to-valve stress \mathbf{f} appearing in (8) is computed from the former, while the latter provides the valve position and velocity. To this aim, we introduce some additional notation related to the representation of the immersed surface Γ_t . Being φ_t a signed distance function, the domain Ω can be partitioned into two open sets

$$\Omega_t^+ = \{\mathbf{x} \in \Omega : \varphi_t(\mathbf{x}) > 0\}, \quad \Omega_t^- = \{\mathbf{x} \in \Omega : \varphi_t(\mathbf{x}) < 0\}. \tag{9}$$

Accordingly, any function f defined over Ω can be decomposed as $f = f^+ + f^-$, where $f^\pm = f|_{\Omega^\pm}$.

Remark 1 (Discontinuity of φ_t) *The definition of φ_t that we employ, implemented in the Visualization Toolkit (VTK, www.vtk.org), yields that $\Gamma_t = \{\mathbf{x} \in \Omega : \varphi_t = 0\}$ is a subset of the interface $\overline{\Omega_t^+} \cap \overline{\Omega_t^-}$ between Ω_t^- and Ω_t^+ . Indeed, as schematically represented in Fig. 2 for a 2D case with a segment Γ , such interface is partitioned into the actual leaflet Γ and the line $(\overline{\Omega^+} \cap \overline{\Omega^-}) \setminus \Gamma$ (a surface in 3D) where φ jumps from negative to positive values.*

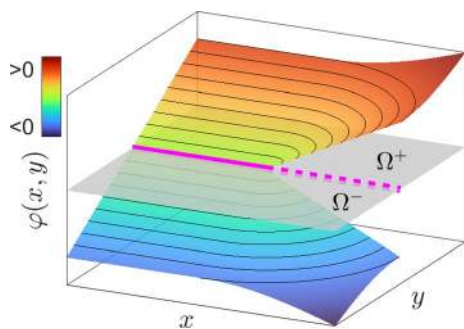


Fig. 2 Two-dimensional sketch of distance function φ for a segment Γ (solid magenta). In gray the plane $\varphi \equiv 0$, with Ω^- and Ω^+ separated by Γ and the discontinuity line (dashed magenta)

The function φ_t allows to define $\tilde{\mathbf{n}}_\Gamma$ and \tilde{H} , that are the extensions to the whole domain Ω of the surface normal \mathbf{n}_Γ and its curvature H , respectively¹:

$$\begin{aligned} \tilde{\mathbf{n}}_\Gamma &= \frac{\nabla \varphi_t}{|\nabla \varphi_t|}, \quad \tilde{H} = -\operatorname{div} \tilde{\mathbf{n}}_\Gamma \\ &= -\frac{\Delta \varphi_t}{|\nabla \varphi_t|} + \frac{\nabla^2 \varphi_t : (\nabla \varphi_t \otimes \nabla \varphi_t)}{|\nabla \varphi_t|^3}, \end{aligned} \quad (10)$$

with $\nabla^2 \varphi_t$ denoting the Hessian matrix of φ_t . The quantities $\tilde{\mathbf{n}}_\Gamma$ and \tilde{H} are actual extensions of the normal vector and curvature, since $\tilde{\mathbf{n}}_\Gamma|_\Gamma = \mathbf{n}_\Gamma, \tilde{H}|_\Gamma = H$ (cf., e.g., (Delfour and Zolésio 2011)). We remark that $\tilde{\mathbf{n}}_\Gamma$ is such that it does not change its verse when passing through Γ_t .

Remark 2 (Normalization) In the definitions (10), we did not make the standard assumption that $|\nabla \varphi_t| \equiv 1$. Indeed, although such an assumption holds in the neighborhood of internal points of Γ_t , its validity is broken near $\partial\Gamma_t$, where φ_t is not continuous. Moreover, this definition of $\tilde{\mathbf{n}}_\Gamma$ ensures that the normal has unit magnitude also at the discrete level.

Regarding the RIIS description of the surface, a definition of the surface velocity \mathbf{u}_Γ is required. Based on the decomposition (6) of the displacement \mathbf{d}_Γ , we provide the following definition:

$$\mathbf{u}_\Gamma(t, \mathbf{x}) = \dot{c}(t)\tilde{\mathbf{g}}(\mathbf{x}), \quad (11)$$

where $\tilde{\mathbf{g}} : \Omega \rightarrow \mathbb{R}^3$ is the closest-point extension of $\mathbf{g} : \hat{\Gamma} \rightarrow \mathbb{R}^3$.

The forces exerted by the fluid on the valve are related to the stress jump across Γ_t , thus

$$\mathbf{f} = [\boldsymbol{\sigma} \mathbf{n}_\Gamma]|_{\Gamma_t} = \boldsymbol{\sigma}^+|_{\Gamma_t} \mathbf{n}_\Gamma - \boldsymbol{\sigma}^-|_{\Gamma_t} \mathbf{n}_\Gamma. \quad (12)$$

Considering the surface smearing introduced by the smooth Dirac delta $\delta_{\Gamma,\epsilon}$ and the definitions (10), the integral term related to \mathbf{f} that appears in (8) can be approximated as follows:

$$\int_{\Gamma_t} \mathbf{f} \cdot \mathbf{n}_\Gamma \approx \int_{\Omega} \left(\boldsymbol{\sigma} \tilde{\mathbf{n}}_\Gamma \cdot \tilde{\mathbf{n}}_\Gamma \delta_{\Gamma,\epsilon}^+ - \boldsymbol{\sigma} \tilde{\mathbf{n}}_\Gamma \cdot \tilde{\mathbf{n}}_\Gamma \delta_{\Gamma,\epsilon}^- \right). \quad (13)$$

Analogously, the other integrals of (8) can be approximated as follows:

$$\begin{aligned} \int_{\Gamma_t} \rho_\Gamma (\mathbf{g} \circ \mathbf{T}_t^{-1}) \cdot \mathbf{n}_\Gamma &\approx \int_{\Omega} \rho_\Gamma (\mathbf{g} \circ \mathbf{T}_t^{-1}) \cdot \tilde{\mathbf{n}}_\Gamma \delta_{\Gamma,\epsilon}, \\ -\gamma \int_{\Gamma_t} \left(H - \hat{H} \circ \mathbf{T}_t^{-1} \right) &\approx -\gamma \int_{\Omega} \left(\tilde{H} - \hat{H} \right) \delta_{\Gamma,\epsilon}, \end{aligned} \quad (14)$$

with \hat{H} denoting the RIIS representation of the pulled-back curvature $\hat{H} \circ \mathbf{T}_t^{-1}$.

Remark 3 (Transvalvular pressure jump) Notice that, since $|\tilde{\mathbf{n}}_\Gamma| \equiv 1$, if the strain component of the normal stress is assumed to be negligible with respect to the pressure term, the integral force in (13) gets down to

$$\int_{\Gamma_t} \mathbf{f} \cdot \mathbf{n}_\Gamma \approx \int_{\Omega} \left(p \delta_{\Gamma,\epsilon}^+ - p \delta_{\Gamma,\epsilon}^- \right), \quad (15)$$

in accordance with other reduced models, such as those proposed by Korakianitis and Shi (2006), Blanco et al. (2010), Seo et al. (2020), Domenichini and Pedrizzetti (2015), which are based on the pressure jump across the valve.

2.4 Numerical approximation

We present the space and time discretization of the coupled 3D-0D FSI model. We introduce a uniform partition of the time interval $[0, T]$ with step-size Δt and nodes $\{t^n = n \Delta t\}_{n=0}^N$. Accordingly, the time-discrete counterparts of all quantities, evaluated at time t^n , will be denoted by a superscript n . For the space discretization, we introduce a hexahedral mesh \mathcal{T}_h for the domain Ω , and the Finite Element (FE) space

$$X_h^r = \left\{ v_h \in C^0(\bar{\Omega}) : v_h|_K \in \mathbb{Q}^r(K), \forall K \in \mathcal{T}_h \right\}, \quad (16)$$

where \mathbb{Q}^r denotes the space of polynomials of degree r with respect to each space coordinate. The velocity and pressure discrete spaces are thus defined as $V_h^r = \{v_h \in [X_h^r]^3 : v_h = \mathbf{0} \text{ on } \Sigma_w\}$ and $Q_h^r = X_h^r$.

For the approximation of the fluid problem (3), we adopt a semi-implicit BDF-FE scheme of order s as done

¹ In view of Remark 1, the derivatives appearing in (10) are computed in Ω^- and Ω^+ separately, so that no contribution actually arises from the discontinuity of φ_t .

by Fedele et al. (2017), with the same polynomial degree r for both V_h^r and Q_h^r and a SUPG-PSPG stabilization with VMS-inspired coefficients: cf. (Forti and Dedè 2015; Bazilevs et al. 2007).

The resulting numerical method reads as follows:

Given $\mathbf{u}_h^n \in V_h^r, n = 0, \dots, s - 1$, for each $n = s, \dots, N$, find $\mathbf{u}_h^n \in V_h^r, p_h^n \in Q_h^r$ such that

$$\begin{aligned} & \left(\rho \frac{\alpha_s \mathbf{u}_h^n - \mathbf{u}_h^{n, \text{BDF}s}}{\Delta t}, \mathbf{v}_h \right) + \bar{a}^n(\mathbf{u}_h^n, \mathbf{v}_h) + c(\mathbf{u}_h^{n,s}, \mathbf{u}_h^n, \mathbf{v}_h) \\ & + b(\mathbf{v}_h, p_h^n) - b(\mathbf{u}_h^n, q_h) \\ & + \sum_{K \in \mathcal{T}_h} (\tau_M^{n,s} \mathbf{r}_M^n(\mathbf{u}_h^n, p_h^n), \rho \mathbf{u}_h^{n,s} \cdot \nabla \mathbf{v}_h + \nabla q_h)_K \\ & + \sum_{K \in \mathcal{T}_h} (\tau_C^{n,s} r_C^n(\mathbf{u}_h^n), \nabla \cdot \mathbf{v}_h)_K = F(\mathbf{v}_h) \end{aligned} \tag{17}$$

for all $\mathbf{v}_h \in V_h^r$ and $q_h \in Q_h^r$, where (\cdot, \cdot) and $(\cdot, \cdot)_K$ denote the L^2 inner product over Ω and a mesh element K , respectively, and

$$\begin{aligned} \bar{a}^n(\mathbf{u}, \mathbf{v}) &= (\mu D(\mathbf{u}), \nabla \mathbf{v}) + \left(\frac{R}{\varepsilon} \mathbf{u} \delta_\varepsilon^n, \mathbf{v} \right), \\ b(\mathbf{v}, q) &= -(\text{div} \mathbf{v}, q), \\ c(\mathbf{w}, \mathbf{u}, \mathbf{v}) &= (\mathbf{w} \cdot \nabla \mathbf{u}, \mathbf{v}), \\ F(\mathbf{v}) &= \int_{\Sigma_{\text{in}}} p_{\text{in}} \mathbf{n} \cdot \mathbf{v} + \int_{\Sigma_{\text{out}}} p_{\text{out}} \mathbf{n} \cdot \mathbf{v} - \left(\frac{R}{\varepsilon} \mathbf{u}_{\Gamma,h}^n \delta_\varepsilon^n, \mathbf{v} \right). \end{aligned}$$

The BDF parameter α_s and the velocities $\mathbf{u}_h^{n, \text{BDF}s}, \mathbf{u}_h^{n,s}$ depend on the order s of the BDF scheme (as in Forti and Dedè (2015)), while $\mathbf{r}_M^n, r_C^n, \tau_M^{n,s}, \tau_C^{n,s}$ are defined as

$$\begin{aligned} \mathbf{r}_M^n(\mathbf{u}_h^n, p_h^n) &= \rho \frac{\alpha_s \mathbf{u}_h^n - \mathbf{u}_h^{n, \text{BDF}s}}{\Delta t} - \mu \Delta \mathbf{u}_h^n + \rho \mathbf{u}_h^{n,s} \cdot \nabla \mathbf{u}_h^n \\ & + \nabla p_h^n + \frac{R}{\varepsilon} \delta_\varepsilon^n (\mathbf{u}_h^n - \mathbf{u}_\Gamma^n), \\ r_C^n(\mathbf{u}_h^n) &= \nabla \cdot \mathbf{u}_h^n, \\ \tau_M^{n,s} &= \left(\frac{\rho^2 \alpha_s^2}{\Delta t^2} + \rho^2 \mathbf{u}_h^{n,s} \cdot \mathfrak{G} \mathbf{u}_h^{n,s} + C_r \mu^2 \mathfrak{G} : \mathfrak{G} + \frac{R^2}{\varepsilon^2} (\delta_\varepsilon^n)^2 \right)^{-1/2}, \\ \tau_C^{n,s} &= (\tau_M^{n,s} \mathfrak{g} \cdot \mathfrak{g})^{-1}. \end{aligned}$$

The quantities \mathfrak{G} and \mathfrak{g} appearing above are the metric tensor and vector, depending on the element map $\mathbf{M}_K : \hat{K} \rightarrow K$, for $K \in \mathcal{T}_h$, mapping the reference element \hat{K} to the current one K (see, e.g., (Tezduyar and Sathe 2003)).

Regarding the geometric quantities describing the valve, we hinge upon a FE description. In particular, the discrete distance function is $\varphi_h^n \in X_h^{r'}$, with a polynomial degree $r' \geq 2$ that is in general different from r . Introducing the basis functions $\{\psi_\ell\}_{\ell=1}^{N_h^{r'}}$ spanning $X_h^{r'}$, the leaflet's extended normal and curvature are defined as follows:

$$\begin{aligned} \tilde{\mathbf{n}}_{\Gamma,h}^n &= \frac{\sum_{\ell=1}^{N_h^{r'}} \varphi_\ell^n \nabla \psi_\ell}{\left| \sum_{\ell=1}^{N_h^{r'}} \varphi_\ell^n \nabla \psi_\ell \right|}, \\ \tilde{H}_{\Gamma,h}^n &= -\text{div} \tilde{\mathbf{n}}_{\Gamma,h}^n \\ &= -\frac{\sum_{\ell=1}^{N_h^{r'}} \varphi_\ell^n \Delta \psi_\ell}{\left| \sum_{\ell=1}^{N_h^{r'}} \varphi_\ell^n \nabla \psi_\ell \right|} \\ & + \frac{\sum_{\ell,m,k=1}^{N_h^{r'}} \varphi_\ell^n \varphi_m^n \varphi_k^n \nabla^2 \psi_\ell : (\nabla \psi_m \otimes \nabla \psi_k)}{\left| \sum_{\ell=1}^{N_h^{r'}} \varphi_\ell^n \nabla \psi_\ell \right|^3} \end{aligned} \tag{18}$$

We point out that, since both these quantities appear in the valve model only as integrands of (13), (14), we can use directly the expressions (18), without the need of a projection onto a finite element space.

Concerning the valve's kinematics, the discrete leaflet velocity is obtained from a first-order approximation of (11):

$$\mathbf{u}_{\Gamma,h}^n = \frac{c^n - c^{n-1}}{\Delta t} \tilde{\mathbf{g}}_h^n, \tag{19}$$

while the solution of the ODE Eq. (8) describing the valve dynamics is based on an explicit fourth-order Runge–Kutta method RK4 (cf. (Süli and Mayers 2003)).

The fluid and structure models are weakly coupled at each time step, as described in the following scheme, graphically displayed in Fig. 3:

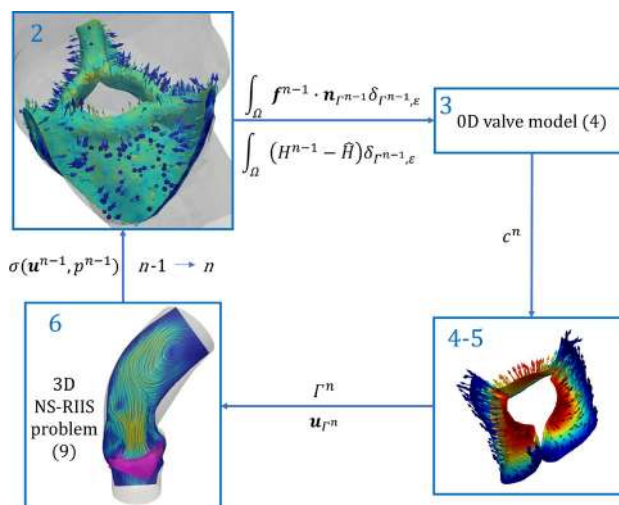


Fig. 3 Graphical representation of the staggered FSI solution scheme: the numbers of the panels correspond to the lines of Algorithm 1. Panel 2: fluid-to-leaflet normal stress $\mathbf{f} \cdot \mathbf{n}$ in the region $\{|\varphi_\Gamma| < \varepsilon\}$. Panel 4–5: leaflet velocity field \mathbf{u}_Γ . Panel 6: blood velocity \mathbf{u} on a slice

Algorithm 1 Solution scheme for the 3D-0D FSI model

Given $\mathbf{u}_h^n, p_h^n, c^n$ for $n = 0, \dots, s - 1$, and computed the functions $\varphi^n, \tilde{\mathbf{n}}_1^n, \tilde{H}^n$ corresponding to the surface Γ^n , for $n = 0, \dots, s - 1$,

- 1: for $n \leftarrow s$ to N do
- 2: Compute the integrals that make up (4), in terms of $\mathbf{u}_h^{n-1}, p_h^{n-1}, \Gamma^{n-1}, \varphi^{n-1}$.
- 3: Find c^n by advancing the 0D equation (4) with a step of RK4.
- 4: Move the immersed surface to its new configuration Γ^n described by $\mathbf{d}_\Gamma^n = c^n \mathbf{g}$ and compute $\mathbf{u}_1^n = \frac{c^n - c^{n-1}}{\Delta t} \tilde{\mathbf{g}}$.
- 5: Compute the new signed distance function φ^n with respect to Γ^n and assemble the normal and curvature fields $\tilde{\mathbf{n}}_1^n$ and \tilde{H}^n .
- 6: Find $(\mathbf{u}_h^n, p_h^n) \in V_h^r \times Q_h^r$ by solving the linear problem (9).
- 7: end for

This solution scheme has been implemented within life^x (cf. (Africa 2022; Africa et al. 2024), <https://lifex.gitlab.io/>), a high-performance parallel C++ library for the solution of multi-physics problems based on the deal.II finite element core described by Arndt et al. (2021).

3 Results and discussion

We show the suitability of the proposed reduced 3D-0D FSI model in describing blood and valve dynamics in the ascending aorta. Both the geometry of the domain Ω and of the closed valve leaflets $\hat{\Gamma}$ are taken from Zygote (cf. (Zygote Media Group, Inc. 2014)), an accurate model of the physiological heart derived from scan acquisitions. To define the open configuration $\Gamma_{\text{open}} = \{\mathbf{x} = \hat{\mathbf{x}} + \mathbf{g}(\hat{\mathbf{x}}), \hat{\mathbf{x}} \in \hat{\Gamma}\}$

—corresponding to an opening coefficient $c = 1$ —we define \mathbf{g} as proportional to the distance field $\tilde{\mathbf{g}}$ connecting each point of a leaflet to the closest point to wall of the corresponding sinus of Valsalva. Specifically, we progressively open the leaflets along $\tilde{\mathbf{g}}$ until a physiological orifice area is attained. The obtained valve configuration is shown in Fig. 1, bottom right and has an orifice area of 2.78 cm², comparable with the values obtained in Johnson et al. (2020). A possible drawback of this approach may be that the total area $|\Gamma_r|$ of the valve is not exactly constant throughout its motion; however, the areas of the fully closed and fully open configuration differ by less than 1%, and all intermediate configurations do not differ from them by more than 6%.

The domain is discretized by a hexahedral mesh of about 100K elements including artificial flow extensions at both inlet and outlet. The elements size h ranges from 2 mm in the flow extensions to 0.5 mm in the aortic root. Blood velocity and pressure are both discretized with \mathbb{Q}^1 finite elements, and a BDF order $s = 1$, namely a semi-implicit Euler scheme, is chosen. The other physical and numerical parameters of the system are reported in Table 1.

Regarding boundary conditions at the inlet and outlet sections of the domain we impose the time-dependent normal stresses $p_{\text{in}}(t), p_{\text{out}}(t)$ displayed in Fig. 4, obtained from the lumped circulation presented by Regazzoni et al. (2022) after proper calibration in order to be consistent with physiological pressures as reported in Wiggers diagrams (see, e.g., (Wiggers 1923)) and comparable with those employed

Table 1 Physical and numerical parameters

ρ [$\frac{\text{kg}}{\text{m}^3}$]	μ [Pa s]	R [Pa s]	ε [m]	ρ_Γ [$\frac{\text{kg}}{\text{m}^2}$]	β [s ⁻¹]	γ [$\frac{\text{N}}{\text{M}}$]	Δt [s]
1060	$3.5 \cdot 10^{-3}$	10^4	10^{-3}	0.265	0.2	3	$2 \cdot 10^{-4}$

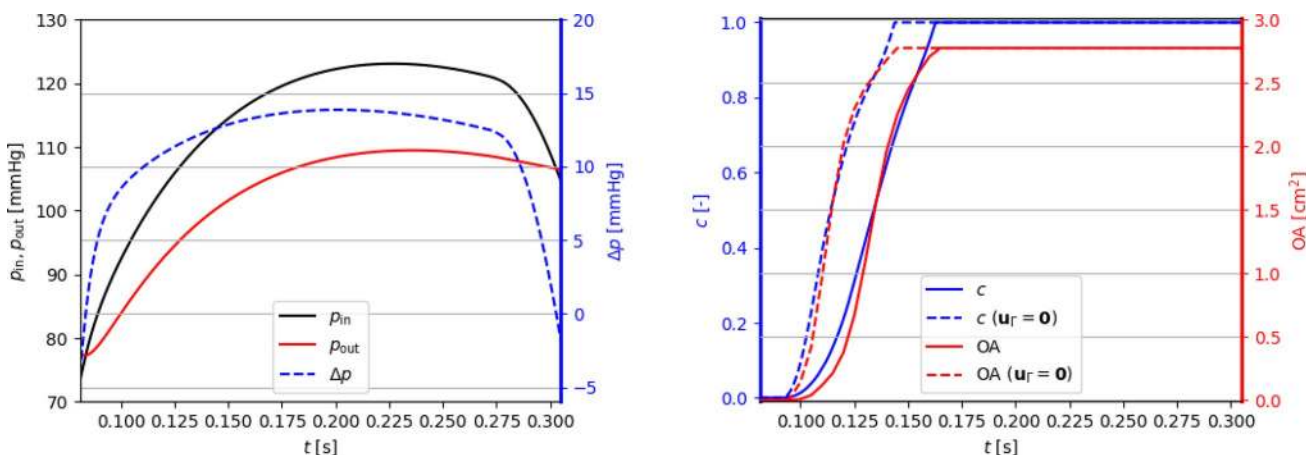


Fig. 4 Physiological pressure boundary conditions (left) and corresponding values of the valve’s opening coefficient c and orifice area (right). The case $\mathbf{u}_r = \mathbf{0}$ is discussed in Sect. 3.2

in computational works such as Kamensky et al. (2015), Johnson et al. (2020).

The choice of an effective calibration strategy is crucial to ensuring that the simulations accurately reflect blood flow physiology around the valve. Despite we did not conduct a systematic sensitivity analysis, we are aware of its importance in this context. Therefore, we explored a partial sensitivity analysis to assess the role of the following parameters in the valve's opening phase:

- The damping parameter β slows down the valve opening phase. Yet, to observe appreciable changes, the value of β should be modified by at least one order of magnitude.
- Increasing γ delays the opening phase and possibly prevents the valve from opening completely. A more detailed discussion is provided in Sect. 3.3.
- An increase in the inertial parameter ρ_Γ is associated with a slowdown of the opening phase. A large increase of this parameter may further reduce the maximum attained orifice area. Further details are discussed in Sect. 3.3.

All the simulations reported in the following were run in parallel on a 48-processor of CINECA's HPC cluster GALILEO100. On average, the wall time for the simulation of a full systole was 5 h. At each time step, the integration of the 3D stress terms on the leaflets and the solution of the reduced valve model required around one-tenth of the computational time employed to solve the flow problem. This shows how the proposed approach introduces little additional computational effort with respect to a purely fluid dynamics simulation.

3.1 Physiological valve opening

We focus on the valve opening phase, from $t = 0.084$ s when the overall pressure difference $\Delta p = p_{\text{in}} - p_{\text{out}}$ between the inlet and the outlet is positive, up to its inversion occurring at $t = 0.302$ s. As we can see from Fig. 4, the opening valve dynamics is characterized by different phases:

- The leaflets remain closed until a minimal transvalvular pressure jump of about 5 mmHg is developed.
- Then, they rapidly open up to their fully open position, in a timespan of 72 ms, in accordance with the measures of 76 ± 30 ms reported by Handke et al. (2003).
- In most part of the systole, the valve remains in its fully open configuration, while the pressure jump progressively decreases.

The evolution of the blood flow during this systolic ejection is reported in Fig. 5. In the early stages of the simulation, while the valve is closed, the whole pressure gradient

is concentrated across the valve. Then, the opening of the valve is accompanied by a progressive development of the typical jet flow through the aortic orifice, and much smaller pressure differences can be observed.

In order to better examine the role of pressure in the valve dynamics, Fig. 5c shows the pressure distribution in the ε -neighborhood of the leaflet, that is in the region where the RIIS term is active. While the valve is closed, the whole pressure gradient develops within that region, showing the effectiveness of the RIIS method in providing an obstacle to the flow. Then, while the valve opens, the pressure jump between the two sides of the leaflets is relatively small, but non-negligible gradients are present inside the RIIS region: This localized inhomogeneity allows to develop a nonzero leaflet velocity \mathbf{u}_Γ while preserving the incompressibility constraint of Navier–Stokes continuity equation. Indeed, when the valve is in its fully open configuration, $\mathbf{u}_\Gamma = \mathbf{0}$ and pressure is essentially constant in the whole ε -neighborhood of Γ_Γ .

3.2 Reconstruction of the leaflet velocity and quasi-static approach

The leaflet velocity \mathbf{u}_Γ is provided by the reduced valve model (19). In this section, we assess its effect on the blood dynamics by comparing our results with those of the quasi-static approach adopted by Fedele et al. (2017). To this aim, a simulation in the same settings and boundary conditions of the previous section is run, the only difference being that $\mathbf{u}_\Gamma = \mathbf{0}$. Resorting to Fig. 4, we can notice that the quasi-static approach entails a faster opening phase (53 ms), with a larger opening velocity \dot{c} especially at the beginning. Moreover, comparing Fig. 6 with Fig. 5, a lower transvalvular pressure gradient can be observed at the early opening stages, as well as a faster developing jet in the aorta. These results can be motivated by observing that, in order to attain $\mathbf{u} = \mathbf{0}$ in the valve region, the continuous function \mathbf{u} must transition from the flow values to 0 in a surrounding boundary layer, which thus artificially enlarges the effective obstacle that the leaflets represent to the flow: As a consequence, the leaflets undergo a stronger push from the flow.

We also compare our results with those of Fedele et al. (2017), in terms of valve opening time. It can be noticed that a much faster opening is observed in that reference (11 ms). This difference is not only in the treatment of the surface velocity \mathbf{u}_Γ , but also in the different valve model considered. We can then state that the model presented in this work represents an improvement in terms of physiological representation of the aortic valve opening. A more detailed comparison with such model is provided in Sect. 3.3.2.

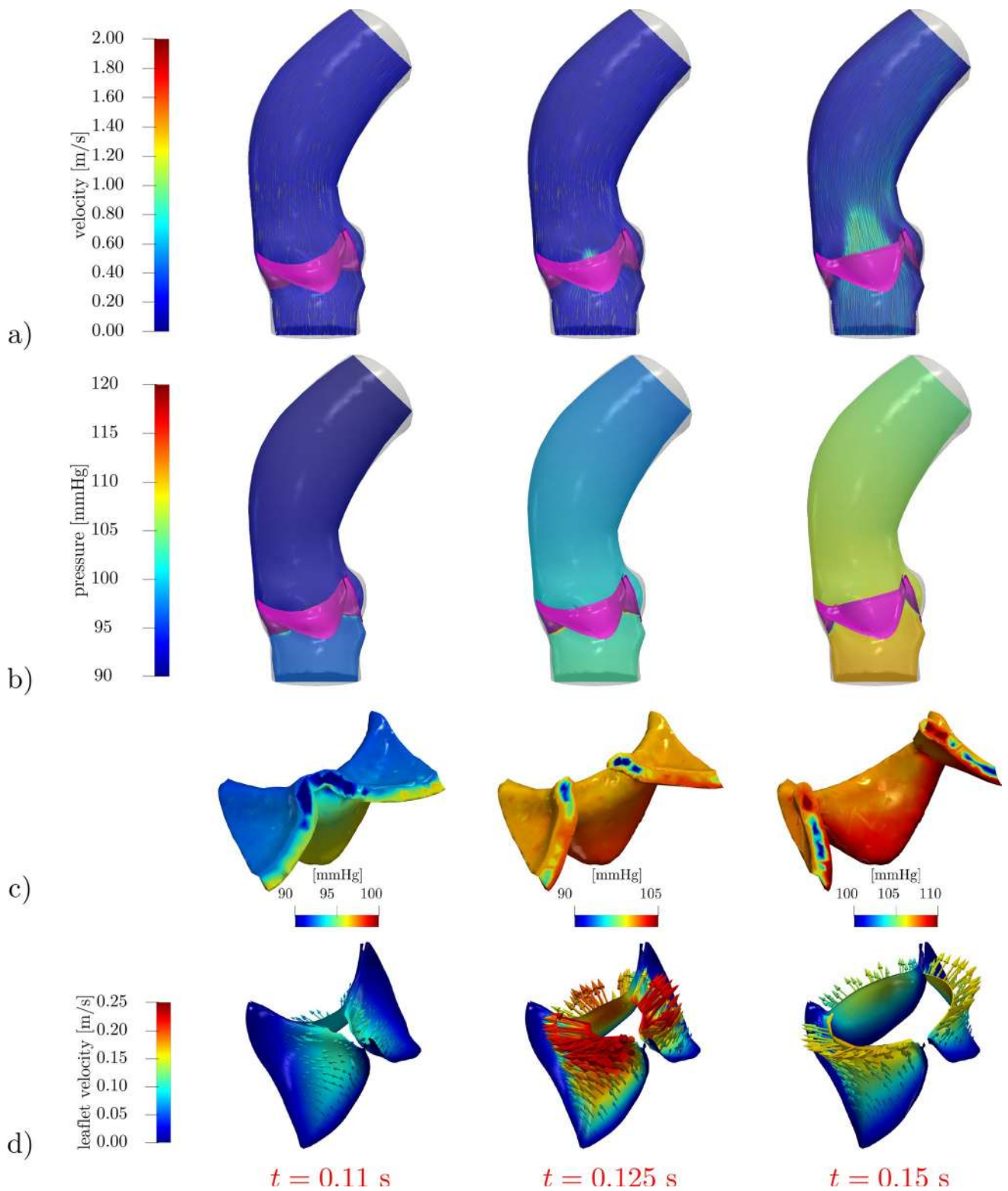


Fig. 5 Velocity (a) and pressure distribution in the domain (b) and within the leaflet region (c) under physiological pressure conditions. Leaflet velocity \mathbf{u}_F in (d). The valve leaflets are colored in purple in (a), (b)

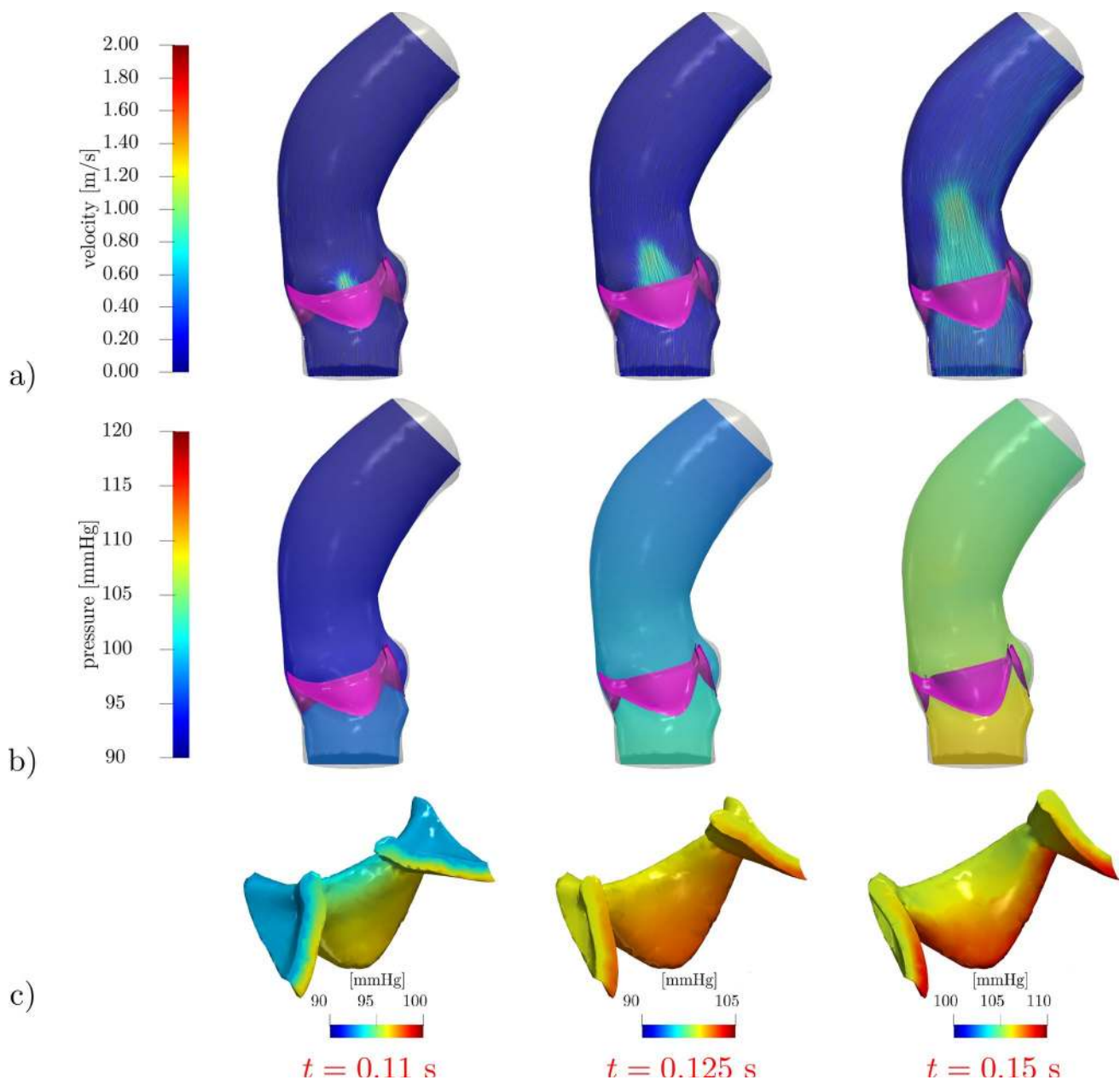


Fig. 6 Quasi-static approach $\mathbf{u}_\Gamma = \mathbf{0}$. Velocity (a) and pressure distribution in the domain (b) and within the leaflet region (c) under physiological pressure conditions. The valve leaflets are colored in purple in (a), (b)

3.3 Full systole: physiological and stenotic valve

We now employ the proposed reduced 3D-0D FSI model to simulate a full systole, with the valve initially closed, namely $c(t=0) = 0$. In view of the discussion of Sect. 3.2, we consider a nonzero leaflet velocity \mathbf{u}_Γ , that is we do not adopt the quasi-static approach. We are going to discuss our numerical results in a physiological case, and then, we will introduce and investigate two different levels of aortic valve stenosis, indicated as *steno-1* and *steno-2* in the following. Specifically, case *steno-1* corresponds to an increase of the

elasticity coefficient γ with respect to the physiological baseline— modeling a stiffening of the valve— and case *steno-2* corresponds to an increase of the parameter ρ_Γ with respect to *steno-1*— modeling an increase of the leaflets' inertia surrogating the added mass of calcifications. The values of γ and ρ_Γ for the different cases are reported in Table 2 together with the following synthetic indicators:

- T_{open} is the time interval between the first time in which $c > 0$ and the first one in which c reaches its maximum value c_{max} ($c_{\text{max}} = 1$ in the physiological case); analo-

Table 2 Synthetic indicators for valve stenosis: physiological, *steno-1*, and *steno-2* cases

		Physio	<i>steno-1</i>	<i>steno-2</i>
γ	[N/m]	3	15	15
ρ_Γ	[kg/m ²]	0.265	0.265	0.276
T_{open}	[ms]	72	58	79
T_{close}	[ms]	32	35	21
OA_{max}	[cm ²]	2.78	1.79	1.06
AS	[%]	0	36	62
U_{peak}	[m/s]	1.52	2.26	2.17
$p_{\text{jump, peak}}$	[mmHg]	3.45	8.41	12.52

gously, T_{close} is the time between the last local maximum of c and the following instant in which $c = 0$;

- the aortic stenosis ratio AS is based on the maximum orifice area OA_{max} : $AS = 1 - \frac{OA_{\text{max}}}{OA_{\text{physio}}}$ (cf. (Seo et al. 2020; Baumgartner et al. 2009)) with OA_{physio} corresponding to the physiological case $\gamma = 3 \text{ N/m}$;
- U_{peak} is the velocity attained by the aortic jet at the end of the opening phase;
- $p_{\text{jump, peak}}$ is the macroscopic pressure jump p_{jump} across the aortic root at the time when U_{peak} is attained. This is computed as $p_{\text{jump}} = p_{\text{up}} - p_{\text{down}}$, where $p_{\text{up}}, p_{\text{down}}$ are the average pressures in two small spheres upwind and downwind to the valve, respectively, as shown in Fig. 8, left.

The baseline settings of the following discussion are those of the physiological case $\gamma = 3 \text{ N/m}$. As displayed in Fig. 7, after the opening phase discussed in Sect. 3.1, the valve remains in its fully open position for 173 ms, and then, it closes in 32 ms. We point out that the duration of the closing phase lays within the physiological range of $42 \pm 16 \text{ ms}$ reported by Handke et al. (2003), even though the calibration procedure considered only the *opening* phase, thus supporting the aptness of the proposed valve model.

The time evolution of the pressure boundary conditions is reported in Fig. 8, together with the cross-valve pressure jump $p_{\text{jump}} = p_{\text{up}} - p_{\text{down}}$. We notice that p_{jump} is definitely positive/negative during the opening/closing phase, whereas it remains below 10 mmHg in the interval $t \in [0.151, 0.336] \text{ s}$ when the valve is fully open. These values are comparable, e.g., with the 5 and 15 mmHg of transvalvular pressure jump reported in Kamensky et al. (2015) and Johnson et al. (2020), respectively. Moreover, the physiological value of the peak velocity $U_{\text{peak}} = 1.52 \text{ m/s}$ —consistent with Hsu et al. (2014)—confirms that the fully open state that we consider corresponds to a non-stenotic configuration.

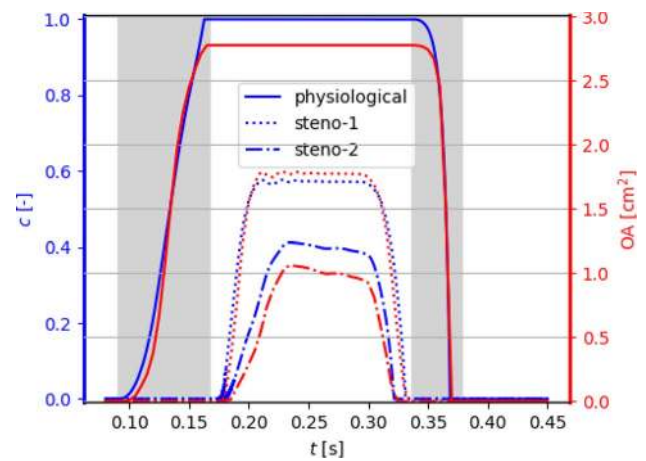


Fig. 7 Opening coefficient c (left axis) and orifice area OA (right axis) under physiological pressure conditions, obtained with the curvature-based model in the case of a physiological valve and two degrees of aortic stenosis (*steno-1*, *steno-2*: see Table 2). The shaded areas correspond to average physiological opening and closing times as reported by Handke et al. (2003)

We notice that the beginning of the closing phase at $t = 0.368 \text{ s}$ is delayed with respect to the inversion of the macroscopic pressure jump, occurring at $t = 0.315 \text{ s}$, and this delay is even larger than the closing time. Such behavior, consistent with the valve modeling literature, is due to the inertia of both the blood flow and the valve, and it shows how the reconstruction of the *local* stress exchanged between the flow and the leaflets has a major impact on the valve dynamics. Indeed, analyzing the time evolutions of Fig. 8, we observe that, in the interval $t \in [0.151, 0.336] \text{ s}$ where $c \equiv 1$, the stress jump $\frac{1}{|\Gamma_i|} \int_{\Gamma_i} \mathbf{f} \cdot \mathbf{n}_\Gamma$ remains between 3 and 5 mmHg, keeping the valve open against the elastic forces; moreover, the change of sign in the stress term occurs at $t = 0.34 \text{ s}$, causing the abovementioned delay of the valve closing phase with respect to the sign inversion of the pressure jump. Furthermore, the average stress jump remains significantly lower than p_{jump} during almost all of the valve-opening phase: This can be seen as a confirmation of the common statement that cardiac valve leaflets (in physiological conditions) are basically *transported* by the flow—as done, e.g., in the purely kinematic model by Colli et al. (2019).

The velocity distribution and the associated coherent vortex structures at different times are displayed in Figs. 10 and 11, respectively. In the valve opening phase, a jet flow is generated, which leads to the formation of the classical ring coherent structures detaching from the tips of the aortic leaflet (see, e.g., (Moore and Dasi 2014; Sotiropoulos et al. 2016; Becsek et al. 2020)), as we can see at $t = 0.2 \text{ s}$ in Fig. 11. The vortex structures are then transported downwind in the ascending aorta during the

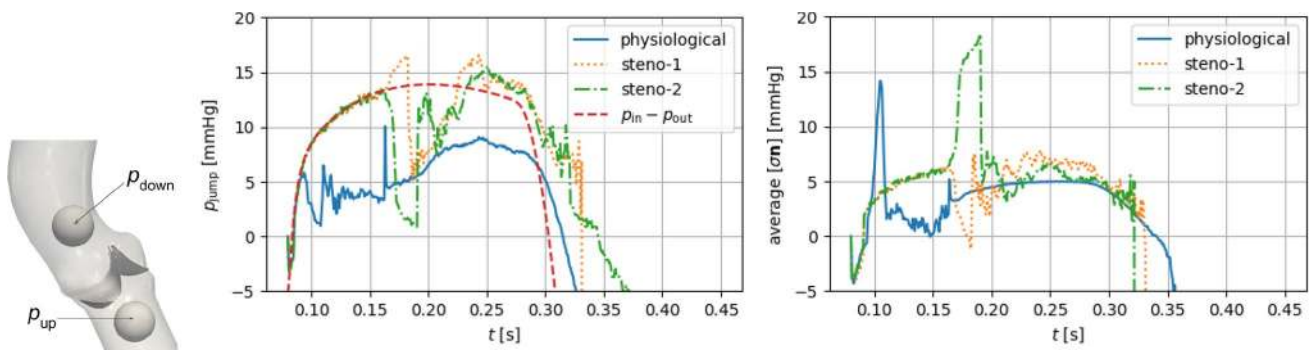


Fig. 8 Full systole: macroscopic pressure jump $p_{\text{jump}} = p_{\text{up}} - p_{\text{down}}$ (center) between two spherical control volumes (left) and transvalvular stress jump $\frac{1}{|\Gamma_r|} \int_{\Gamma_r} \mathbf{f} \cdot \mathbf{n}_{\Gamma}$ (right). The overall pressure difference $\Delta p = p_{\text{in}} - p_{\text{out}}$ is reported, too, for comparison

valve opening phase and the jet breaks up as soon as the valve is fully open (see Fig. 11, $t = 0.2 - 0.3$ s). Finally, after the valve is closed, residual flow recirculations can be appreciated both upstream and downstream to the valve.

To assess the effectiveness of the RIIS penalty method in representing a non-leaking valve, in Fig. 9, we report the flowrate Q_{AV} through a transversal section of the whole domain, together with a zoom on p_{jump} when the valve is closed. By comparison with Fig. 7, we can notice that the flowrate is very small when the valve is closed: the maximum of $|Q_{\text{AV}}|$ when $c = 0$ corresponds to a spurious regurgitation of 4.2 ml/s (attained at $t = 0.41$ s), when the valve sustains a negative pressure jump $p_{\text{jump}}|_{t=0.41\text{s}} \simeq -98$ mmHg, comparable with Hsu et al. (2015). Before the valve is fully closed, instead, in the last part of the closing phase, we can observe a backflow that reaches 296 ml/s: This is due to the valve inertia, and it is in partial accordance with the backflow of ~ 200 ml/s observed in the same phase in Hsu et al. (2014);

Kamensky et al. (2015), where a detailed 3D valve model is considered.

3.3.1 Modeling a stenotic valve

According to the literature, a calcification-based stenosis of the aortic valve is associated with a reduced compliance of the leaflets, which thus oppose a higher resistance to the blood flow (cf., e.g., (Carabello and Paulus 2009)). This feature can be included in our reduced model by increasing the stiffness parameter γ , that can be used to model different degrees of stenosis severity. Moreover, the added mass of the calcifications increases the leaflets' inertia. In this section, we compare the physiological valve with the cases *steno-1* and *steno-2* introduced at the beginning of Sect. 3.3. The chosen values of γ and ρ_{Γ} are reported in Table 2 together with the synthetic indicators defined above.

The time evolution of the opening coefficient c and of the orifice area, displayed in Fig. 7 and summarized in Table 2, shows how both an increase in γ and in ρ_{Γ} yields a reduction

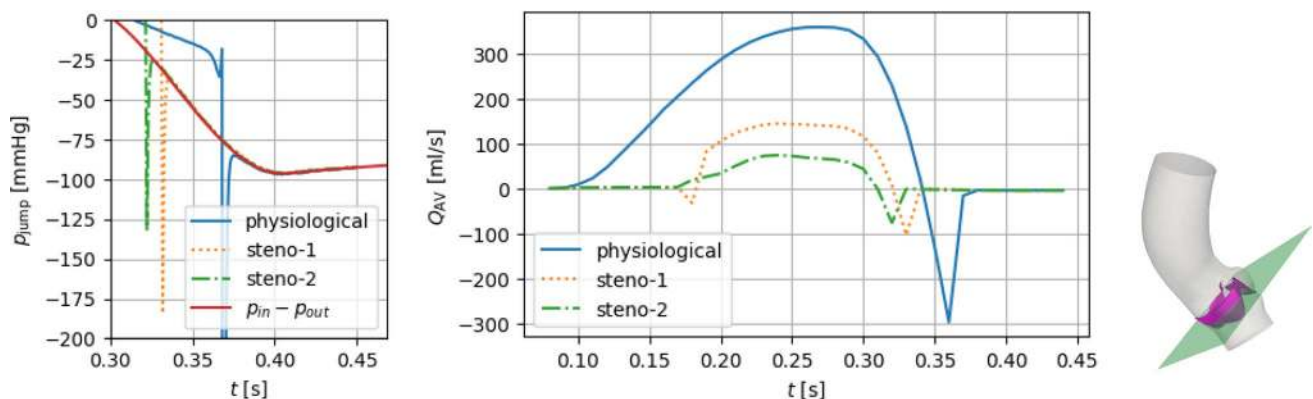


Fig. 9 Evolution of p_{jump} when the valve is closing and fully closed (left), and of the flowrate Q_{AV} throughout the whole systole (center). On the right, the section through which Q_{AV} is computed, transversally crossing the whole domain

of the maximum achievable opening of the valve, with an opening phase that is slower in case *steno-1*. Indeed, from Fig. 8, we can observe that p_{jump} in the stenotic cases has an almost doubled average value than the physiological cases, and it even exceeds, in the closing phase, the maximum pressure difference $p_{\text{in}} - p_{\text{out}}$ that is imposed as a boundary condition over the whole domain. As already pointed out in Sect. 3.1, the control-volume-based macroscopic pressure jump p_{jump} stems from a combination of the *local* stress term $\int_{\Gamma} \mathbf{f} \cdot \mathbf{n}_{\Gamma}$ and the elastic term $\gamma \int_{\Gamma} (H - \hat{H})$. Indeed, the stress term is comparatively small in the closing phase, which is dominated by the elastic forces, while in the opening phase it shows great variability among the three different settings considered here.

In terms of peak velocity U_{peak} , we notice higher values in the stenotic cases, with values of more than 2 m/s and thus exceeding the physiological range. Yet, we point out that, as confirmed by the routine clinical practice (see, e.g., (Baumgartner et al. 2009)), a single indicator for stenosis may not be sufficient to fully categorize a patient’s condition, and different indicators have to be considered at the same time. Indeed, although the values of AS may indicate that *steno-1* and *steno-2* are representative of mild and moderate stenosis, respectively (see (Seo et al. 2020; Baumgartner et al. 2009)), the indicators U_{peak} and $p_{\text{jump,peak}}$ both lie in the mild stenosis range.

In Figs. 10 and 11, we report the velocity field on a 2D slice and the coherent vortex structures generated by the Q-criterion method (cf. (Hunt et al. 1988)). We notice that, in the stenosis cases, the reduced orifice area and the shorter time interval in which flow is allowed through the valve yield a stronger aortic jet and a more disorganized velocity distribution. The ring vortex detaching from the tips of the leaflets, that can be seen at time $t = 0.20$ s, is highly distorted in a short time (see $t = 0.25 - 0.30$ s), while it is transported along the jet and impacts on the posterior aortic wall. After valve closure (see $t = 0.40$ s), the smaller blood velocity magnitude and vortical structure dimensions in the stenotic cases indicate a less effective mixing of blood and a longer residence time of blood in this portion of the vessel, thus yielding a reduced cardiac output. Moreover, since *steno-2* represents a more stenotic case than *steno-1*, the jet that can be appreciated in Fig. 10c, albeit characterized by high velocity values, gets very narrow and lasts for less than half of the systole. Correspondingly, the velocity profile is more chaotic, and the vortical structures undergo a faster breakdown into small-scale eddies (cfr. Fig. 11b, c).

3.3.2 Comparison with the Korakianitis–Shi model

We compare the proposed curvature-based reduced model with another 3D-0D FSI system proposed by Fedele et al.

(2017). In that reference, a Navier–Stokes–RIIS fluid dynamics system is coupled with the Korakianitis–Shi (KS) model for leaflet mechanics introduced by Korakianitis and Shi (2006):

$$\ddot{\theta} + k_f \dot{\theta} = (k_p p_{\text{jump}} + k_b Q) \cos \theta - k_v |Q| \sin(2\theta), \quad (20)$$

where θ is the valve opening angle, ranging between some prescribed values $\theta_{\text{min}}, \theta_{\text{max}}$, and it depends on the pressure jump p_{jump} and the flowrate Q across the valve; $k_{(\cdot)}$ are model parameters that need calibration. Hinging upon the definition of the resistance area introduced by Korakianitis and Shi (2006), Fedele et al. (2017)

$$\text{AR}_{\text{ao}} = \frac{(1 - \cos \theta)^2}{(1 - \cos \theta_{\text{max}})^2} \quad (21)$$

and observing that the orifice area is quadratic with respect to the opening coefficient c ranging from 0 to 1, the opening angle $\theta(t)$ can be related to $c(t)$ by

$$c(t) = \frac{\cos \theta_{\text{min}} - \cos \theta(t)}{\cos \theta_{\text{min}} - \cos \theta_{\text{max}}}. \quad (22)$$

In reference (Fedele et al. 2017), a patient-specific geometry was analyzed, and a quasi-static approach was adopted in the RIIS term, that is $\mathbf{u}_{\Gamma} = \mathbf{0}$ is considered in the momentum equation. In view of the discussion of Sect. 3.2, we drop here the quasi-static hypothesis: This and the difference in the geometry of interest lead us to a re-calibration of the KS model. Consistently with what done for the proposed curvature-based 0D model, the calibration was carried out aiming at a physiological opening time, and the resulting model parameters are reported in Table 3.

The time evolution of the opening coefficient and the associated effective orifice area are displayed in Fig. 12, and synthetic indicators are reported in Table 4. We notice that the resulting KS model does not allow a full opening of the valve, with a maximum angle $\theta = 66^\circ < \theta_{\text{max}}$, although both the opening and closing times T_{open} and T_{close} lie in the physiological ranges 76 ± 30 ms and 46 ± 12 ms, respectively. The latter observation may be seen as an improvement with respect to Fedele et al. (2017), which reported a slow closing phase, that can be ascribed to considering the velocity surface \mathbf{u}_{Γ} . The lack of reaching a fully open position, in turn, is due to the choice made on the calibration strategy: In additional numerical tests, we observed that modifying the parameters to attain a larger maximum value of θ would determine a non-physiologically short opening time (an observation in accordance with Fedele et al. (2017)).

In Fig. 13, we report the velocity distribution and coherent vortical structures obtained in these settings. Comparing such results with those of Figs. 10 and 11, we notice that that they are intermediate between the physiological and *steno-1*

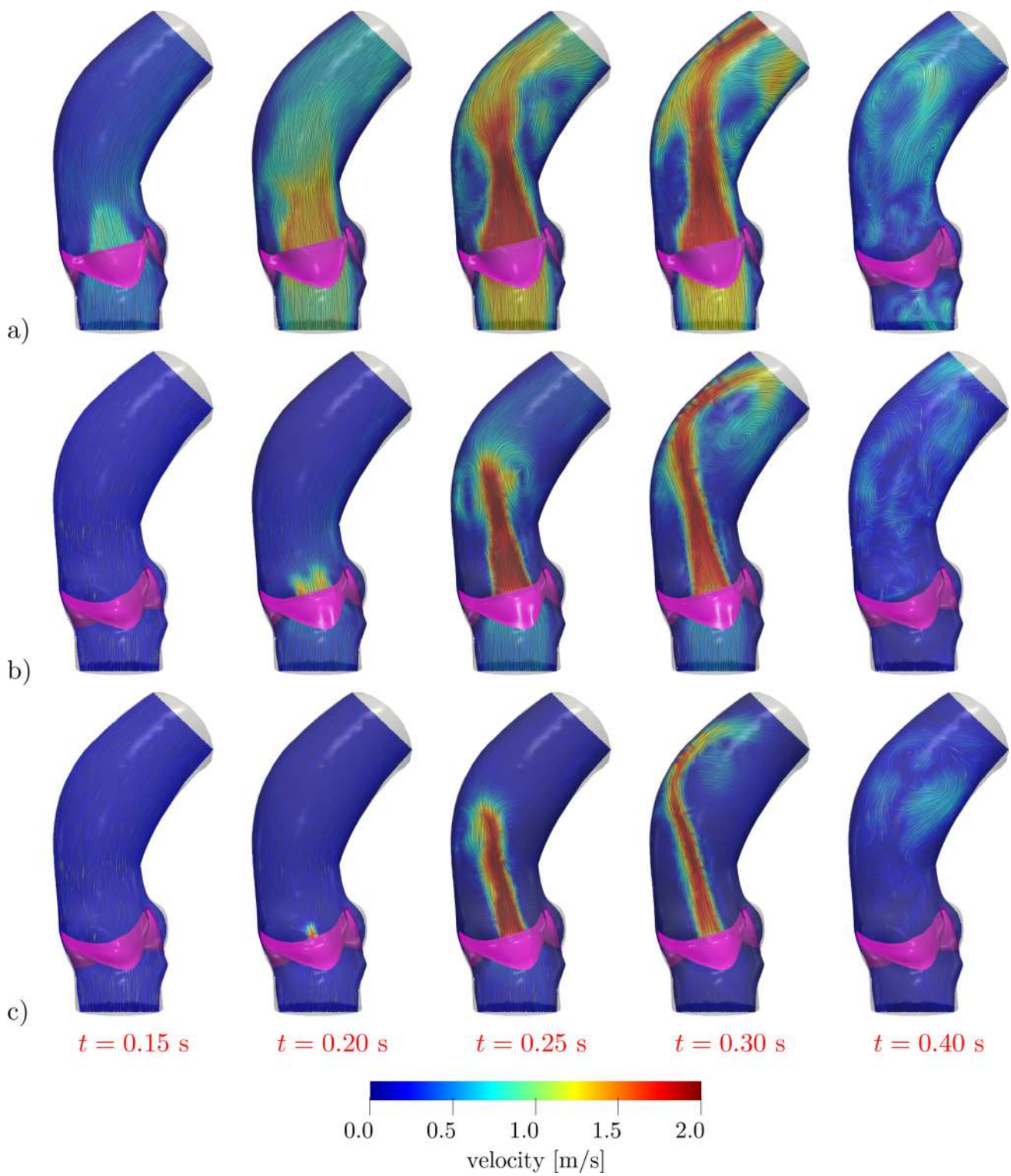


Fig. 10 Velocity distribution on a longitudinal slice at different times: **a** physiological case, **b** case *steno-1*, **c** case *steno-2* (see Table 2)

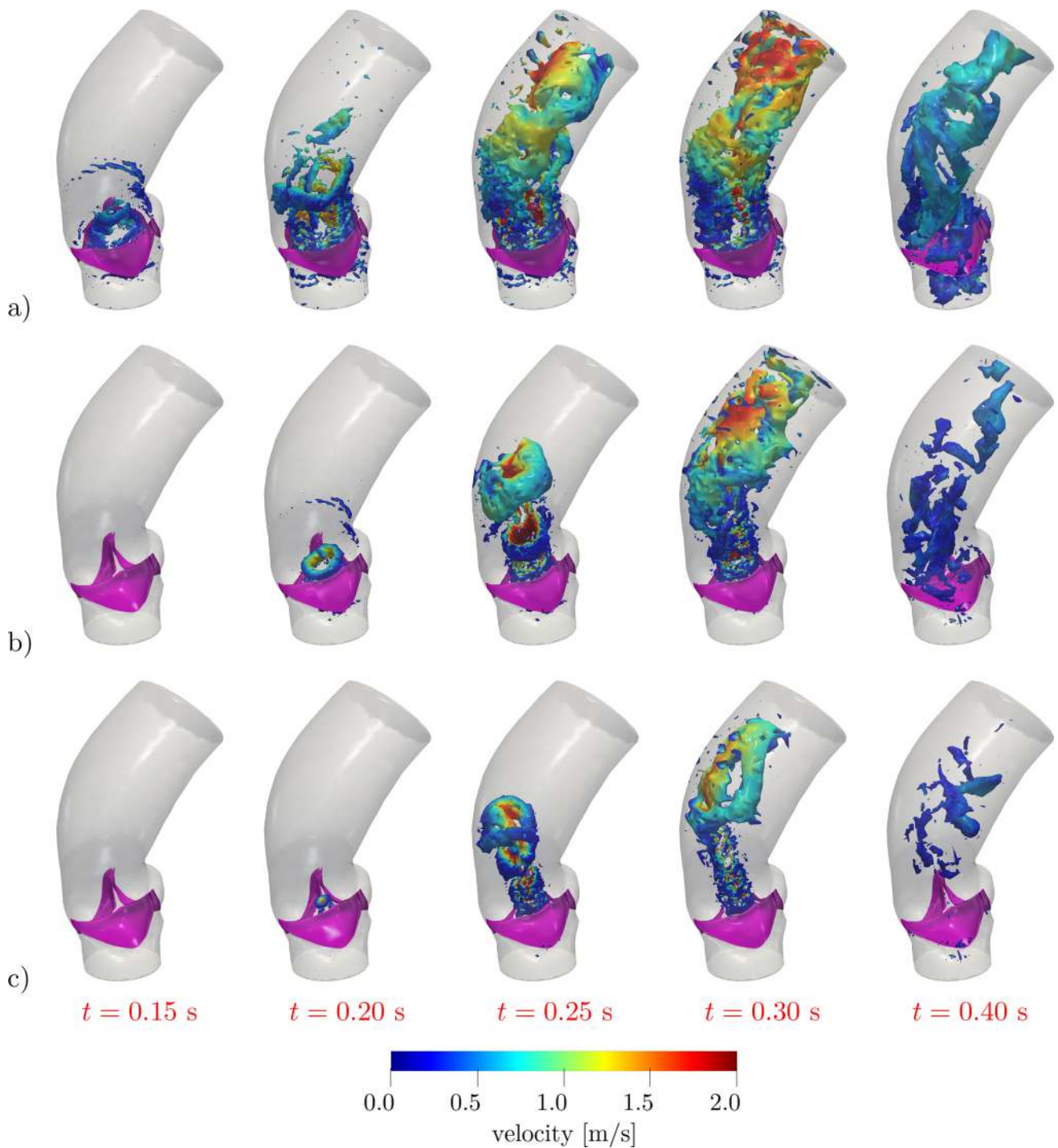


Fig. 11 Q-criterion isosurfaces with $Q = 5000 \text{ s}^{-2}$ colored with velocity magnitude at different times: **a** physiological case, **b** case *steno-1*, **c** case *steno-2* (see Table 2)

Table 3 Model parameters for the KS model

k_f	k_p	k_b	k_v	θ_{\min}	θ_{\max}
$\left[\frac{\text{rad}}{\text{s}} \right]$	$\left[\frac{\text{rad}}{\text{mmHg s}^2} \right]$	$\left[\frac{\text{rad}}{\text{mL}} \right]$	$\left[\frac{\text{rad}}{\text{mL}} \right]$	$[^\circ]$	$[^\circ]$
50	665	6	21	5	75

cases of the curvature-based model, as it is for the stenosis indicators AS and U_{peak} reported in Table 4. This confirms that the KS model, when calibrated in order to attain physiological opening times, leads to a slightly stenotic behavior of the valve.

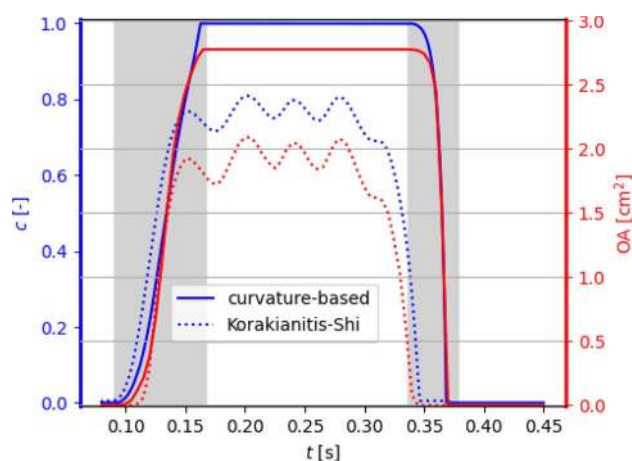


Fig. 12 Full systole: opening coefficient c (left axis) and orifice area OA (right axis) under physiological pressure conditions, obtained with the curvature-based model and with the KS model

Table 4 Synthetic indicators for valve stenosis for the curvature-based model proposed here and the one by Korakianitis and Shi

		Curvature-based	KS
γ	[N/m]	3	–
T_{open}	[ms]	72	64
T_{close}	[ms]	32	52
OA_{max}	[cm ²]	2.78	2.10
AS	[%]	0	24
U_{peak}	[m/s]	1.52	1.78
$p_{\text{jump, peak}}$	[mmHg]	3.45	5.98

4 Conclusions

We proposed a novel reduced FSI model for the aortic valve. The valve dynamics was described by a lumped-parameter model considering the flow-induced stress and a curvature-based elasticity term, as well as damping effects, and its coupling with the 3D blood flow was based on the RIIS method. This system was employed to simulate the blood flow in the ascending aorta, both in physiological conditions and in the case of mild aortic stenosis.

The numerical results demonstrate that the proposed model is a computationally efficient approach for simulating aortic hemodynamics and the effects of valve dynamics on blood flow. Compared to a CFD simulation with prescribed leaflet displacement, the additional computational effort cost is minimal, limited to the assembly of the right-hand side of the ODE governing valve dynamics, which can be efficiently carried out at each quadrature node. The model also straightforwardly provides an explicit expression for the leaflets' velocity \mathbf{u}_Γ , without resorting to complex reconstruction procedures that would introduce discrete interpolation

errors. The comparison with a quasi-static approach adopted in previous works and with the Korakianitis–Shi model showed the advantages of our model in reconstructing the surface velocity and reproducing a physiological duration of the valve opening and closing phases.

To achieve the computational efficiency of the proposed method, we introduced some assumptions that may limit its applicability. Although accounting for macroscopic curvature changes in the leaflets, the model does not fully describe local deformations nor leaflet coaptation or prolapse. Moreover, we assume uniform material properties, ignoring the heterogeneity of stiffness and thickness and the anisotropy of the tissue, which may impact valve dynamics. For these reasons, in several applications, a reduced model such as the one proposed is not a substitute for a fully three-dimensional fluid–structure model. The latter approach is necessary to have an accurate description of mechanical stresses in the leaflets and a locally detailed stress–strain relationship, as needed, e.g., in the investigation of the onset and progression of valve calcification or structural degeneration. Moreover, a fully detailed modeling is required to analyze flow details in proximity of the leaflets and shear stress distributions, associated with thrombotic risk, or to capture leaflet fluttering, which is the subject of increasing investigation, especially in prosthetic valve design. Finally, our reduced model does not allow to predict long-term biomechanical changes related to valve disease progression, remodeling or degeneration.

Nevertheless, our model could be employed as an agile computational tool for several hemodynamics investigations. Since it includes the valve geometry, it can provide a more realistic representation of transvalvular pressure gradients and flow features compared to lumped-parameter models. It could be used in scenario analysis for the assessment of the hemodynamics effects of valve stenosis in domains including the ventricle or a wider downstream tract of the aorta and proximal vessels, where the computational burden of a fully 3D model may become impractical. Indeed, a preliminary step in this direction has been taken in the investigation of pulmonary valve replacement (Criseo et al. 2024). Furthermore, it could be employed in population-based studies, where computational efficiency is paramount.

In order to further enhance the proposed model for the study of different scenarios and pathological conditions, different directions of research may be undertaken. A more precise representation of the valve's open configuration could be achieved using patient-specific imaging data. Moreover, the opening field \mathbf{g} could be replaced by a more complex displacement field involving additional (though still limited) degrees of freedom, as in Domenichini and Pedrizzetti (2015). This could improve the conservation of the valve's mass throughout its dynamics and possibly account for additional kinematic modes in a synthetic way.

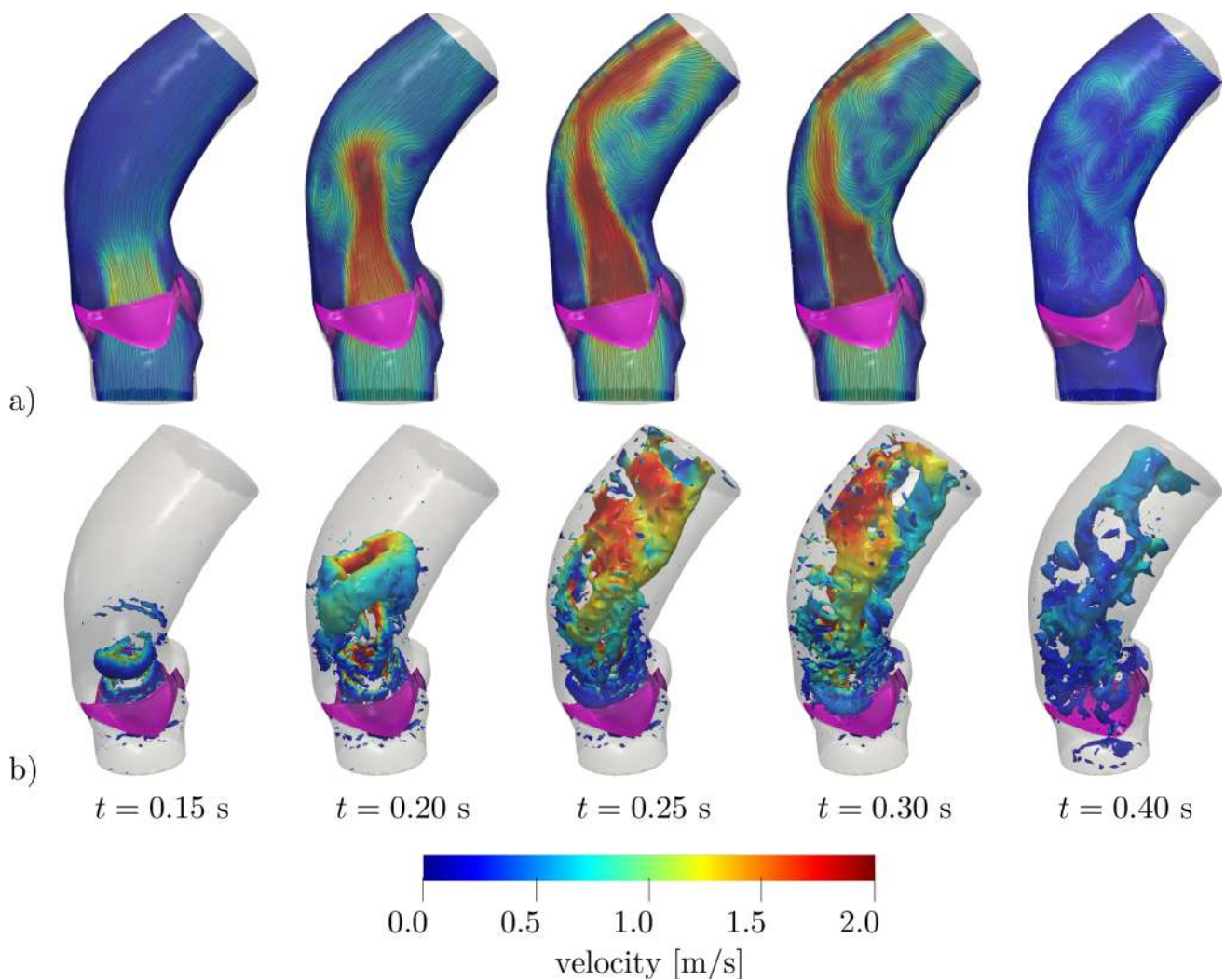


Fig. 13 Results with Korakianitis–Shi model at different times: **a** velocity distribution on a longitudinal slice; **b** Q-criterion isosurfaces with $Q = 5000 \text{ s}^{-2}$ colored with velocity magnitude

An efficient semi-automatic calibration strategy of the model parameters would allow a patient-specific analysis of different pathological conditions, as well as the simulation of possible treatment scenarios to help the pre-operative design. In such context, the efficiency of the calibration procedure would have particular relevance: Reduced order models and machine-learning-based surrogates of this complex system may thus help in this respect. Thanks to the general derivation of the model from a local force balance, its extension to the pulmonary valve of even the atrioventricular valves can be envisaged, possibly introducing additional terms accounting for the subvalvular apparatus.

In terms of the numerical scheme, an implicit coupling of the fluid and valve model could be considered. While this would increase computational cost, adopting a semi-implicit strategy, as proposed in Hsu et al. (2015) and

Johnson et al. (2020), could help mitigate the additional effort.

Finally, an additional level of complexity may be introduced by considering contact forces exchanged among the leaflets, that may affect the dynamics in the early opening phase and in diastole.

Acknowledgements LD acknowledges funding from the HORIZON-EUROHPC-JU-2023-COE-03 project dealii-X “an Exascale Framework for Digital Twins of the Human Body” (no. 101172493). We gratefully acknowledge the CINECA award under the ISCR C initiative for the availability of high performance computing resources and support in the project HP10C794N5 (P.I. I. Fumagalli). All the authors are members of the INdAM group GNCS “Gruppo Nazionale per il Calcolo Scientifico” (National Group for Scientific Computing). The present research is part of the activities of “Dipartimento di Eccellenza 2023-2027,” MUR, Italy, Dipartimento di Matematica, Politecnico di Milano. We also acknowledge the anonymous reviewers

for their insightful comments, which greatly contributed to improving the present work.

Author contributions I.F. wrote the first draft of the manuscript and developed the methodology and software. All authors contributed to the work conceptualization and reviewed the manuscript. A.Q. and L.D. provided funding.

Funding Open access funding provided by Politecnico di Milano within the CRUI-CARE Agreement. This work received funding from the European Research Council (ERC) under the European Union's Horizon Europe research and innovation programme (grant agreement No 101172493, dealii-X).

Data availability No datasets were generated or analyzed during the current study.

Declarations

Competing interests The authors have not disclosed any competing interests.

Open Access This article is licensed under a Creative Commons Attribution 4.0 International License, which permits use, sharing, adaptation, distribution and reproduction in any medium or format, as long as you give appropriate credit to the original author(s) and the source, provide a link to the Creative Commons licence, and indicate if changes were made. The images or other third party material in this article are included in the article's Creative Commons licence, unless indicated otherwise in a credit line to the material. If material is not included in the article's Creative Commons licence and your intended use is not permitted by statutory regulation or exceeds the permitted use, you will need to obtain permission directly from the copyright holder. To view a copy of this licence, visit <http://creativecommons.org/licenses/by/4.0/>.

References

- Africa PC (2022) lifex: a flexible, high performance library for the numerical solution of complex finite element problems. *SoftwareX* 20:101252. <https://doi.org/10.1016/j.softx.2022.101252>
- Africa PC, Fumagalli I, Bucelli M, Zingaro A, Fedele M, Dede' L, Quarteroni A (2024) lifex-cfd: an open-source computational fluid dynamics solver for cardiovascular applications. *Comput Phys Commun* 296:109039. <https://doi.org/10.1016/j.cpc.2023.109039>
- Alauzet F, Fabrèges B, Fernández MA, Landajuela M (2016) Nitsche-XFEM for the coupling of an incompressible fluid with immersed thin-walled structures. *Comput Methods Appl Mech Eng* 301:300–335. <https://doi.org/10.1016/j.cma.2015.12.015>
- Arndt D, Bangerth W, Blais B, Fehling M, Gassmüller R, Heister T, Heltai L, Köcher U, Kronbichler M, Maier M et al (2021) The deal.II library, version 9.3. *J Numer Math* 29(3):171–186. <https://doi.org/10.1515/jnma-2021-0081>
- Astorino M, Gerbeau J-F, Pantz O, Traore K-F (2009) Fluid-structure interaction and multi-body contact: application to aortic valves. *Comput Methods Appl Mech Eng* 198(45–46):3603–3612. <https://doi.org/10.1016/j.cma.2008.09.012>
- Astorino M, Hamers J, Shadden SC, Gerbeau J-F (2012) A robust and efficient valve model based on resistive immersed surfaces. *Int J Numer Methods Biomed Eng* 28(9):937–959. <https://doi.org/10.1002/cnm.2474>
- Basting S, Quaini A, Čanić S, Glowinski R (2017) Extended ALE method for fluid-structure interaction problems with large structural displacements. *J Comput Phys* 331:312–336. <https://doi.org/10.1016/j.jcp.2016.11.043>
- Baumgartner H, Hung J, Bermejo J, Chambers JB, Evangelista A, Griffin BP, Iung B, Otto CM, Pellikka PA, Quiñones M (2009) Echocardiographic assessment of valve stenosis: EAE/ASE recommendations for clinical practice. *J Am Soc Echocardiogr* 22(1):1–23. <https://doi.org/10.1016/j.echo.2008.11.029>
- Bazilevs Y, Calo VM, Cottrell JA, Hughes TJR, Reali A, Scovazzi G (2007) Variational multiscale residual-based turbulence modeling for large eddy simulation of incompressible flows. *Comput Methods Appl Mech Eng* 197(1–4):173–201. <https://doi.org/10.1016/j.cma.2007.07.016>
- Bazilevs Y, Hsu M-C, Kiendl J, Wüchner R, Bletzinger K-U (2011) 3D simulation of wind turbine rotors at full scale. Part II: Fluid-structure interaction modeling with composite blades. *Int J Numer Methods Fluids* 65(1–3):236–253. <https://doi.org/10.1002/flid.2454>
- Becsek B, Pietrasanta L, Obrist D (2020) Turbulent systolic flow downstream of a bioprosthetic aortic valve: velocity spectra, wall shear stresses, and turbulent dissipation rates. *Front Physiol* 11:1169
- Bellhouse B (1969) Velocity and pressure distributions in the aortic valve. *J Fluid Mech* 37(3):587–600. <https://doi.org/10.1017/S0022112069000747>
- Blanco PJ, Feijóo RA et al (2010) A 3D-1D-0D computational model for the entire cardiovascular system. *Comput Mech* 29:5887–5911
- Bonomi D, Vergara C, Faggiano E, Stevanella M, Conti C, Redaelli A, Puppini G, Faggian G, Formaggia L, Luciani GB (2015) Influence of the aortic valve leaflets on the fluid-dynamics in aorta in presence of a normally functioning bicuspid valve. *Biomech Model Mechanobiol* 14(6):1349–1361. <https://doi.org/10.1007/s10237-015-0679-8>
- Borzajani I, Ge L, Sotiropoulos F (2008) Curvilinear immersed boundary method for simulating fluid structure interaction with complex 3D rigid bodies. *J Comput Phys* 227(16):7587–7620. <https://doi.org/10.1016/j.jcp.2008.04.028>
- Borzajani I, Ge L, Sotiropoulos F (2010) High-resolution fluid-structure interaction simulations of flow through a bi-leaflet mechanical heart valve in an anatomic aorta. *Ann Biomed Eng* 38(2):326–344. <https://doi.org/10.1007/s10439-009-9807-x>
- Burman E, Fernández MA (2014) An unfitted Nitsche method for incompressible fluid-structure interaction using overlapping meshes. *Comput Methods Appl Mech Eng* 279:497–514. <https://doi.org/10.1016/j.cma.2014.07.007>
- Buscaglia GC, Ausas RF (2011) Variational formulations for surface tension, capillarity and wetting. *Comput Methods Appl Mech Eng* 200(45–46):3011–3025. <https://doi.org/10.1016/j.cma.2011.06.002>
- Carabello BA, Paulus WJ (2009) Aortic stenosis. *Lancet* 373(9667):956–966. [https://doi.org/10.1016/S0140-6736\(09\)60211-7](https://doi.org/10.1016/S0140-6736(09)60211-7)
- Causin P, Gerbeau J-F, Nobile F (2005) Added-mass effect in the design of partitioned algorithms for fluid-structure problems. *Comput Methods Appl Mech Eng* 194(42–44):4506–4527. <https://doi.org/10.1016/j.cma.2004.12.005>
- Cheng R, Lai YG, Chandran KB (2004) Three-dimensional fluid-structure interaction simulation of bileaflet mechanical heart valve flow dynamics. *Ann Biomed Eng* 32(11):1471–1483
- Chnafa C, Mendez S, Nicoud F (2014) Image-based large-eddy simulation in a realistic left heart. *Comput Fluids* 94:173–187. <https://doi.org/10.1016/j.compfluid.2014.01.030>
- Chnafa C, Mendez S, Nicoud F (2016) Image-based simulations show important flow fluctuations in a normal left ventricle: what could be the implications? *Ann Biomed Eng* 44(11):3346–3358. <https://doi.org/10.1007/s10439-016-1614-6>

- Collia D, Vukicevic M, Meschini V, Zovatto L, Pedrizzetti G (2019) Simplified mitral valve modeling for prospective clinical application of left ventricular fluid dynamics. *J Comput Phys* 398:108895. <https://doi.org/10.1016/j.jcp.2019.108895>
- Criseo E, Fumagalli I, Quarteroni A, Marianeschi SM, Vergara C (2024) Computational haemodynamics for pulmonary valve replacement by means of a reduced fluid–structure interaction model. *Int J Numer Methods Biomed Eng* 40(9):3846. <https://doi.org/10.1002/cnm.3846>
- De Hart J, Peters G, Schreurs P, Baaijens F (2003) A three-dimensional computational analysis of fluid–structure interaction in the aortic valve. *J Biomech* 36(1):103–112. [https://doi.org/10.1016/s0021-9290\(02\)00244-0](https://doi.org/10.1016/s0021-9290(02)00244-0)
- Dedè L, Menghini F, Quarteroni A (2019) Computational fluid dynamics of blood flow in an idealized left human heart. *Int J Numer Methods Biomed Eng* 37(11):3287. <https://doi.org/10.1002/cnm.3287>
- Delfour MC, Zolésio J-P (2011) Shapes and geometries: metrics, analysis, differential calculus, and optimization. SIAM, Soc Ind Appl Math. <https://doi.org/10.1137/1.9780898719826>
- Domenichini F, Pedrizzetti G (2015) Asymptotic model of fluid–tissue interaction for mitral valve dynamics. *Cardiovasc Eng Technol* 6(2):95–104. <https://doi.org/10.1007/s13239-014-0201-y>
- Dos Santos ND, Gerbeau J-F, Bourgat J-F (2008) A partitioned fluid–structure algorithm for elastic thin valves with contact. *Comput Methods Appl Mech Eng* 197(19–20):1750–1761. <https://doi.org/10.1016/j.cma.2007.03.019>
- El Sabbagh A, Reddy YN, Nishimura RA (2018) Mitral valve regurgitation in the contemporary era: insights into diagnosis, management, and future directions. *JACC Cardiovasc Imaging* 11(4):628–643. <https://doi.org/10.1016/j.jcmg.2018.01.009>
- Espino DM, Shepherd DE, Hukins DW (2014) Evaluation of a transient, simultaneous, arbitrary Lagrange–Euler based multiphysics method for simulating the mitral heart valve. *Comput Methods Biomech Biomed Eng* 17(4):450–458. <https://doi.org/10.1080/10255842.2012.688818>
- Fedele M, Faggiano E, Dedè L, Quarteroni A (2017) A patient-specific aortic valve model based on moving resistive immersed implicit surfaces. *Biomech Model Mechanobiol* 16(5):1779–1803. <https://doi.org/10.1007/s10237-017-0919-1>
- Fernández MA, Gerbeau J-F, Martin V (2008) Numerical simulation of blood flows through a porous interface. *ESAIM Math Model Numer Anal* 42(6):961–990. <https://doi.org/10.1051/m2an:2008031>
- Formaggia L, Vergara C, Zonca S (2018) Unfitted extended finite elements for composite grids. *Comput Math Appl*. <https://doi.org/10.1016/j.camwa.2018.05.028>
- Forti D, Dedè L (2015) Semi-implicit BDF time discretization of the Navier–Stokes equations with VMS–LES modeling in a high performance computing framework. *Comput Fluids* 117:168–182. <https://doi.org/10.1016/j.compfluid.2015.05.011>
- Fumagalli I, Vergara C (2024) Novel approaches for the numerical solution of fluid–structure interaction in the aorta. In: Gasser TC, Avril S, Elefteriades JA (eds) *Biomechanics of the Aorta. Biomechanics of living organs*. Academic Press, Cambridge, pp 347–385. <https://doi.org/10.1016/B978-0-323-95484-6.00017-8>
- Fumagalli I, Parolini N, Verani M (2018) On a free-surface problem with moving contact line: from variational principles to stable numerical approximations. *J Comput Phys* 355:253–284. <https://doi.org/10.1016/j.jcp.2017.11.004>
- Fumagalli I, Fedele M, Vergara C, Dedè L, Ippolito S, Nicolò F, Antona C, Scrofani R, Quarteroni A (2020) An image-based computational hemodynamics study of the systolic anterior motion of the mitral valve. *Comput Biol Med* 123:103922. <https://doi.org/10.1016/j.combiomed.2020.103922>
- Fumagalli I, Vitullo P, Vergara C, Fedele M, Corno AF, Ippolito S, Scrofani R, Quarteroni A (2022) Image-based computational hemodynamics analysis of systolic obstruction in hypertrophic cardiomyopathy. *Front Physiol* 12:787082. <https://doi.org/10.3389/fphys.2021.787082>
- Ge L, Sotiropoulos F (2010) Direction and magnitude of blood flow shear stresses on the leaflets of aortic valves: is there a link with valve calcification? *J Biomech Eng* 132(1):014505. <https://doi.org/10.1115/1.4000162>
- Ge L, Leo H-L, Sotiropoulos F, Yoganathan AP (2005) Flow in a mechanical bileaflet heart valve at laminar and near-peak systole flow rates: CFD simulations and experiments. *J Biomech Eng* 127(5):782–797. <https://doi.org/10.1115/1.1993665>
- Gerstenberger A, Wall WA (2008) An eXtended Finite Element Method/Lagrange multiplier based approach for fluid–structure interaction. *Comput Methods Appl Mech Eng* 197(19–20):1699–1714. <https://doi.org/10.1016/j.cma.2007.07.002>
- Gerstenberger A, Wall W (2010) An embedded Dirichlet formulation for 3D continua. *Int J Numer Meth Eng* 82(5):537–563. <https://doi.org/10.1002/nme.2755>
- Glowinski R, Pan T-W, Periaux J (1997) A Lagrange multiplier/fictitious domain method for the numerical simulation of incompressible viscous flow around moving rigid bodies:(I) case where the rigid body motions are known a priori. *Comptes Rendus de l'Académie des Sci Series I-Math* 324(3):361–369. [https://doi.org/10.1016/S0764-4442\(99\)80376-0](https://doi.org/10.1016/S0764-4442(99)80376-0)
- Griffith BE (2012) Immersed boundary model of aortic heart valve dynamics with physiological driving and loading conditions. *Int J Numer Methods Biomed Eng* 28(3):317–345. <https://doi.org/10.1002/cnm.1445>
- Griffith BE, Luo X, McQueen DM, Peskin CS (2009) Simulating the fluid dynamics of natural and prosthetic heart valves using the immersed boundary method. *Int J Appl Mech* 1(01):137–177. <https://doi.org/10.1142/S1758825109000113>
- Handke M, Heinrichs G, Beyersdorf F, Olschewski M, Bode C, Geibel A (2003) In vivo analysis of aortic valve dynamics by transesophageal 3-dimensional echocardiography with high temporal resolution. *J Thorac Cardiovasc Surg* 125(6):1412–1419. [https://doi.org/10.1016/S0022-5223\(02\)73604-0](https://doi.org/10.1016/S0022-5223(02)73604-0)
- Hansbo P, Larson MG, Zahedi S (2015) Characteristic cut finite element methods for convection–diffusion problems on time dependent surfaces. *Comput Methods Appl Mech Eng* 293:431–461. <https://doi.org/10.1016/j.cma.2015.05.010>
- Hsu M-C, Kamensky D, Bazilevs Y, Sacks MS, Hughes TJR (2014) Fluid–structure interaction analysis of bioprosthetic heart valves: significance of arterial wall deformation. *Comput Mech* 54(4):1055–1071. <https://doi.org/10.1007/s00466-014-1059-4>
- Hsu M-C, Kamensky D, Xu F, Kiendl J, Wang C, Wu MC, Mineroff J, Reali A, Bazilevs Y, Sacks MS (2015) Dynamic and fluid–structure interaction simulations of bioprosthetic heart valves using parametric design with t-splines and fung-type material models. *Comput Mech* 55:1211–1225
- Hughes TJR, Hulbert GM (1988) Space–time finite element methods for elastodynamics: formulations and error estimates. *Comput Methods Appl Mech Eng* 66(3):339–363. [https://doi.org/10.1016/0045-7825\(88\)90006-0](https://doi.org/10.1016/0045-7825(88)90006-0)
- Hunt J, Wray A, Moin P (1988) Eddies, streams, and convergence zones in turbulent flows. Center for Turbulence Research Report CTR-S88, pp 193–208
- Jianhai Z, Dapeng C, Shengquan Z (1996) ALE finite element analysis of the opening and closing process of the artificial mechanical valve. *Appl Math Mech* 17(5):403–412. <https://doi.org/10.1007/BF00131088>
- Johnson EL, Wu MC, Xu F, Wiese NM, Rajanna MR, Herrema AJ, Ganapathysubramanian B, Hughes TJ, Sacks MS, Hsu M-C (2020) Thinner biological tissues induce leaflet

- flutter in aortic heart valve replacements. *Proc Natl Acad Sci* 117(32):19007–19016
- Kaiser AD, Shad R, Hiesinger W, Marsden AL (2021) A design-based model of the aortic valve for fluid-structure interaction. *Biomech Model Mechanobiol* 20(6):2413–2435
- Kamensky D, Hsu M-C, Schillinger D, Evans JA, Aggarwal A, Bazilevs Y, Sacks MS, Hughes TJR (2015) An immersogeometric variational framework for fluid-structure interaction: application to bioprosthetic heart valves. *Comput Methods Appl Mech Eng* 284:1005–1053. <https://doi.org/10.1016/j.cma.2014.10.040>
- Korakianitis T, Shi Y (2006) Numerical simulation of cardiovascular dynamics with healthy and diseased heart valves. *J Biomech* 39(11):1964–1982. <https://doi.org/10.1016/j.jbiomech.2005.06.016>
- Kunzelman K, Cochran R (1990) Mechanical properties of basal and marginal mitral valve chordae tendineae. *ASAIO Trans* 36(3):405–8
- Le TB, Sotiropoulos F (2013) Fluid-structure interaction of an aortic heart valve prosthesis driven by an animated anatomic left ventricle. *J Comput Phys* 244:41–62. <https://doi.org/10.1016/j.jcp.2012.08.036>
- Liu WK, Liu Y, Farrell D, Zhang L, Wang XS, Fukui Y, Patankar N, Zhang Y, Bajaj C, Lee J et al (2006) Immersed finite element method and its applications to biological systems. *Comput Methods Appl Mech Eng* 195(13–16):1722–1749. <https://doi.org/10.1016/j.cma.2005.05.049>
- Loon R, Anderson PD, Vosse FN (2006) A fluid-structure interaction method with solid-rigid contact for heart valve dynamics. *J Comput Phys* 217(2):806–823. <https://doi.org/10.1016/j.jcp.2006.01.032>
- Marom G (2015) Numerical methods for fluid-structure interaction models of aortic valves. *Arch Comput Methods Eng* 22(4):595–620. <https://doi.org/10.1007/s11831-014-9133-9>
- Marom G, Peleg M, Halevi R, Rosenfeld M, Raanani E, Hamdan A, Haj-Ali R (2013) Fluid-structure interaction model of aortic valve with porcine-specific collagen fiber alignment in the cusps. *J Biomech Eng* 135(10):101001. <https://doi.org/10.1115/1.4024824>
- Massing A, Larson M, Logg A, Rognes M (2015) A Nitsche-based cut finite element method for a fluid-structure interaction problem. *Commun Appl Math Comput Sci* 10(2):97–120. <https://doi.org/10.2140/camcos.2015.10.97>
- Mayer UM, Popp A, Gerstenberger A, Wall WA (2010) 3D fluid-structure-contact interaction based on a combined XFEM FSI and dual mortar contact approach. *Comput Mech* 46(1):53–67. <https://doi.org/10.1007/s00466-010-0486-0>
- Mihalef V, Ionasec RI, Sharma P, Georgescu B, Voigt I, Suehling M, Comaniciu D (2011) Patient-specific modelling of whole heart anatomy, dynamics and haemodynamics from four-dimensional cardiac CT images. *Interface Focus* 1(3):286–296. <https://doi.org/10.1098/rsfs.2010.0036>
- Moore B, Dasi LP (2014) Spatiotemporal complexity of the aortic sinus vortex. *Exp Fluids* 55(7):1–12. <https://doi.org/10.1007/s00348-014-1770-0>
- Moore KL, Dalley AF, Agur AM (2013) Clinically oriented anatomy. Lippincott Williams & Wilkins, Philadelphia
- Morganti S, Auricchio F, Benson D, Gambarin F, Hartmann S, Hughes T, Reali A (2015) Patient-specific isogeometric structural analysis of aortic valve closure. *Comput Methods Appl Mech Eng* 284:508–520
- Morsi YS, Yang WW, Wong CS, Das S (2007) Transient fluid-structure coupling for simulation of a trileaflet heart valve using weak coupling. *J Artif Organs* 10(2):96–103. <https://doi.org/10.1007/s10047-006-0365-9>
- Nestola MGC, Faggiano E, Vergara C, Lancellotti RM, Ippolito S, Antona C, Filippi S, Quarteroni A, Scrofani R (2017) Computational comparison of aortic root stresses in presence of stentless and stented aortic valve bio-prostheses. *Comput Methods Biomech Biomed Eng* 20(2):171–181. <https://doi.org/10.1080/10255842.2016.1207171>
- Nestola MGC, Becsek B, Zolfaghari H, Zulian P, De Marinis D, Krause R, Obrist D (2019) An immersed boundary method for fluid-structure interaction based on variational transfer. *J Comput Phys* 398:108884. <https://doi.org/10.1016/j.jcp.2019.108884>
- Otto CM (2008) Calcific aortic stenosis-time to look more closely at the valve. *Mass Medical Soc.* <https://doi.org/10.1056/NEJMe0807001>
- Peskin CS (1972) Flow patterns around heart valves: a numerical method. *J Comput Phys* 10(2):252–271. [https://doi.org/10.1016/0021-9991\(72\)90065-4](https://doi.org/10.1016/0021-9991(72)90065-4)
- Quarteroni A, Dede L, Manzoni A, Vergara C (2019) Mathematical modelling of the human cardiovascular system-data, numerical approximation. In: *Clinical applications*, Cambridge University Press, Cambridge
- Regazzoni F, Salvador M, Africa P, Fedele M, Dedè L, Quarteroni A (2022) A cardiac electromechanical model coupled with a lumped-parameter model for closed-loop blood circulation. *J Comput Phys* 457:111083. <https://doi.org/10.1016/j.jcp.2022.111083>
- Rim Y, McPherson DD, Kim H (2014) Effect of leaflet-to-chordae contact interaction on computational mitral valve evaluation. *Biomed Eng Online* 13(1):31. <https://doi.org/10.1186/1475-925X-13-31>
- Schievano S, Coats L, Migliavacca F, Norman W, Frigiola A, Deanfield J, Bonhoeffer P, Taylor AM (2007) Variations in right ventricular outflow tract morphology following repair of congenital heart disease: implications for percutaneous pulmonary valve implantation. *J Cardiovasc Magn Reson* 9(4):687–695. <https://doi.org/10.1080/10976640601187596>
- Schoen FJ (2005) Cardiac valves and valvular pathology: update on function, disease, repair, and replacement. *Cardiovasc Pathol* 14(4):189–194. <https://doi.org/10.1016/j.carpath.2005.03.005>
- Seo JH, Vedula V, Abraham T, Lardo AC, Dawoud F, Luo H, Mittal R (2014) Effect of the mitral valve on diastolic flow patterns. *Phys Fluids* 26(12):121901. <https://doi.org/10.1063/1.4904094>
- Seo J-H, Zhu C, Resar J, Mittal R (2020) Flow physics of normal and abnormal bioprosthetic aortic valves. *Int J Heat Fluid Flow* 86:108740. <https://doi.org/10.1016/j.ijheatfluidflow.2020.108740>
- Sotiropoulos F, Le TB, Gilmanov A (2016) Fluid mechanics of heart valves and their replacements. *Ann Rev Fluid Mech* 48:259–283. <https://doi.org/10.1146/annurev-fluid-122414-034314>
- Stijnen J, De Hart J, Bovendeerd P, Vosse F (2004) Evaluation of a fictitious domain method for predicting dynamic response of mechanical heart valves. *J Fluids Struct* 19(6):835–850. <https://doi.org/10.1016/j.jfluidstructs.2004.04.007>
- Süli E, Meyers DF (2003) An introduction to numerical analysis. Cambridge University Press, Cambridge. <https://doi.org/10.1017/CBO9780511801181>
- Tagliabue A, Dedè L, Quarteroni A (2017) Fluid dynamics of an idealized left ventricle: the extended Nitsche’s method for the treatment of heart valves as mixed time varying boundary conditions. *Int J Numer Meth Fluids* 85(3):135–164. <https://doi.org/10.1002/flid.4375>
- Tagliabue A, Dedè L, Quarteroni A (2017) Complex blood flow patterns in an idealized left ventricle: a numerical study. *Chaos Int J Nonlinear Sci* 27(9):093939. <https://doi.org/10.1063/1.5002120>
- Takizawa K, Tezduyar TE, Terahara T, Sasaki T (2018) Heart valve flow computation with the space-time slip interface topology change (ST-SI-TC) method and isogeometric analysis (IGA). In:

- Biomedical technology, pp. 77–99, Springer, Cham. https://doi.org/10.1007/978-3-319-59548-1_6
- Tezduyar T, Sathe S (2003) Stabilization parameters in SUPG and PSPG formulations. *J Comput Appl Mech* 4(1):71–88
- Tezduyar TE, Sathe S (2007) Modelling of fluid–structure interactions with the space–time finite elements: solution techniques. *Int J Numer Meth Fluids* 54(6–8):855–900. [https://doi.org/10.1016/0045-7825\(88\)90006-0](https://doi.org/10.1016/0045-7825(88)90006-0)
- This A, Morales HG, Bonnefous O, Fernández MA, Gerbeau J-F (2020) A pipeline for image based intracardiac CFD modeling and application to the evaluation of the PISA method. *Comput Methods Appl Mech Eng* 358:112627. <https://doi.org/10.1016/j.cma.2019.112627>
- Thubrikar M (2018) *The aortic valve*. Routledge, New York. <https://doi.org/10.4324/9780203737163>
- Viscardi F, Vergara C, Antiga L, Merelli S, Veneziani A, Puppini G, Faggian G, Mazzucco A, Luciani GB (2010) Comparative finite element model analysis of ascending aortic flow in bicuspid and tricuspid aortic valve. *Artif Organs* 34(12):1114–1120. <https://doi.org/10.1111/j.1525-1594.2009.00989.x>
- Votta E, Le TB, Stevanella M, Fusini L, Caiani EG, Redaelli A, Sotiropoulos F (2013) Toward patient-specific simulations of cardiac valves: state-of-the-art and future directions. *J Biomech* 46(2):217–228. <https://doi.org/10.1016/j.jbiomech.2012.10.026>
- Wiggers CJ (1923) *Modern aspects of the circulation in health and disease*. Lea & Febiger, Philadelphia
- Wu MC, Zakerzadeh R, Kamensky D, Kiendl J, Sacks MS, Hsu M-C (2018) An anisotropic constitutive model for immersogeometric fluid–structure interaction analysis of bioprosthetic heart valves. *J Biomech* 74:23–31. <https://doi.org/10.1016/j.jbiomech.2018.04.012>
- Xanthos T, Dalivigkas I, Ekmektzoglou KA (2011) Anatomic variations of the cardiac valves and papillary muscles of the right heart. *IJAE Ital J Anat Embryol* 116:111–126
- Yang J, Yu F, Krane M, Zhang LT (2018) The perfectly matched layer absorbing boundary for fluid–structure interactions using the immersed finite element method. *J Fluids Struct* 76:135–152. <https://doi.org/10.1016/j.jfluidstruct.2017.09.002>
- Zahle F, Sørensen NN, Johansen J (2009) Wind turbine rotor–tower interaction using an incompressible overset grid method. *Wind Energy Int J Progress Appl Wind Power Convers Technol* 12(6):594–619. <https://doi.org/10.1002/we.327>
- Zingaro A, Dede' L, Menghini F, Quarteroni A (2021) Hemodynamics of the heart's left atrium based on a variational multiscale–LES numerical method. *Eur J Mech B/Fluids* 89:380–400. <https://doi.org/10.1016/j.euromechflu.2021.06.014>
- Zingaro A, Fumagalli I, Dede' L, Fedele M, Africa PC, Corno AF, Quarteroni A (2022) A geometric multiscale model for the numerical simulation of blood flow in the human left heart. *Discrete Contin Dyn Syst*. <https://doi.org/10.3934/dcdss.2022052>
- Zonca S, Vergara C, Formaggia L (2018) An unfitted formulation for the interaction of an incompressible fluid with a thick structure via an XFEM/DG approach. *SIAM J Sci Comput* 40(1):59–84. <https://doi.org/10.1137/16M1097602>
- Zygote Media Group, Inc.: Zygote solid 3D heart generation II development report. Technical report (2014)

Publisher's Note Springer Nature remains neutral with regard to jurisdictional claims in published maps and institutional affiliations.